Contact sites between endoplasmic reticulum sheets and mitochondria regulate mitochondrial DNA replication and segregation

Hema Saranya Ilamathi[1,2,3], Sara Benhammouda[1,2,3], Amel Lounas[4], Khalid Al-Naemi[5], Justine Desrochers-Goyette[1,2,3], Matthew A. Lines[6], François J. Richard[4], Jackie Vogel[5], Marc Germain[1,2,3#]

[1]Groupe de Recherche en Signalisation Cellulaire and Département de Biologie Médicale, Université du Québec à Trois-Rivières, Trois-Rivières, Québec, Canada

[2]Centre d'Excellence en Recherche sur les Maladies Orphelines - Fondation Courtois, Université du Québec à Montréal, Montréal, Québec, Canada

[3]Réseau Intersectoriel de Recherche en Santé de l'Université du Québec (RISUQ)

[4]Centre de Recherche en Reproduction, Développement et Santé Intergénérationnelle (CRDSI), Département des Sciences Animales, Faculté des Sciences de L'agriculture et de L'alimentation, Université Laval, Québec, Canada.

[5]Departement of Biology, McGill University, Montréal, Québec, Canada

[6]Department of Medical Genetics, Cumming School of Medicine, University of Calgary, Calgary, Alberta, Canada

 # Correspondence: Marc Germain (marc.germain1@uqtr.ca)

Abstract

Mitochondria are multi-faceted organelles crucial for cellular homeostasis that contain their own genome. Mitochondrial DNA (mtDNA) codes for several essential components of the electron transport chain, and mtDNA maintenance defects lead to mitochondrial diseases. mtDNA replication occurs at endoplasmic reticulum (ER)-mitochondria contact sites and is regulated by mitochondrial dynamics. Specifically, mitochondrial fusion is essential for mtDNA maintenance. In contrast, while loss of mitochondrial fission causes the aggregation of nucleoids (mtDNA-protein complexes), its role in nucleoid distribution remains unclear. Here, we show that contact sites between mitochondria and ER sheets, the ER structure associated with protein synthesis, regulate mtDNA replication and nucleoid distribution within mitochondrial networks. Specifically, DRP1 loss or mutation leads to altered ER sheets and enhanced physical interaction with mitobulbs, mitochondrial structures containing aggregated nucleoids. Importantly, nucleoid distribution and mtDNA replication were rescued by expressing the ER sheet protein CLIMP63. Thus, our work identifies a novel role of ER sheets-mitochondria contact sites in regulating mtDNA replication and distribution.

Keywords: mtDNA, DRP1, fission, ER sheets, mitochondria, contact site, nucleoid

Introduction

Mitochondria are dynamic organelles regulating an array of cellular processes including energy production, cellular metabolism, apoptosis, calcium signaling, ROS signaling, cellular differentiation, and immune response against pathogens (*1-6*). These mitochondrial functions are regulated by mitochondrial dynamics, the processes of mitochondrial fusion and fission. Mitochondrial fission requires DRP1 (Dynamin-Related Protein 1) (*7, 8*), while fusion is regulated by Mitofusins 1 and 2 (MFN1 & 2) and Optic Atrophy Protein 1 (OPA1) present on mitochondrial outer and inner membrane respectively (*9, 10*). Mitochondrial dynamics are also essential for mitochondrial DNA (mtDNA) maintenance, with defects in mitochondrial fusion affecting mtDNA integrity and copy number (*11, 12*). On the other hand, while defective mitochondrial fission does not generally affect overall mtDNA content, it alters the distribution of nucleoids (mtDNA-protein complexes), leading to the formation of bulb-like mitochondrial structures termed mitobulbs (*13-16*). Importantly, both mitochondrial fission and mtDNA replication are initiated at sites of contact between mitochondria and the endoplasmic reticulum (ERMCS)(*17-19*), indicating a crucial role for the ER in the regulation of mitochondrial structure and function.

The ER is a complex web-like organelle that includes flattened cisternae/sheets mostly around the perinuclear region and tubulated structures towards the cellular periphery (*20*). Rough ER (rER) generally adopts a sheets-like structure that is enriched with ribosomes and regulates the production and assembly of proteins for secretion (*21*). On the other hand, smooth ER (sER) is usually present as tubulated structures that play important roles in lipid synthesis and calcium signaling, but also in mitochondrial dynamics and mtDNA replication (*17-19, 21*). At the molecular level, the ER resident protein CLIMP63 (CKAP4) is essential for the stabilizing ER sheets, while reticulons (RTN) and DP1/Yop1p are essential for both ER tubule formation and the maintenance of ER sheet curvature (*22, 23*). The ratio of sheet to tubule proteins regulates the balance between the two ER structures (*22*).

Specific membrane proteins present on the ER and mitochondria tether the two organelles to form ERMCS. These interorganelle tethers play key roles in the regulation of mitochondrial dynamics, mtDNA replication, calcium signaling, lipid metabolism and transfer, innate immune response, and autophagy (*17-19, 24-28*). As ERMCS have mainly been reported at ER tubules, we have limited knowledge of the role of ER sheets in ERMCS formation and function. One of the few examples of ER sheet-mitochondria contact sites occurs in mouse liver cells where these ERMCS regulate lipid metabolism (*29, 30*). Nevertheless, the role of ER sheets-mitochondria contact sites in mitochondrial biogenesis is poorly understood.

Here, we show that altered ER sheet-mitochondria interaction disrupts mtDNA replication and segregation. Specifically, mutation or deletion of DRP1 alters ER sheet structure and increases ER sheet interaction with mitochondria, leading to a reduction in mtDNA replication and segregation. Importantly, modulating ER sheets through the expression of CLIMP63 normalized ER sheets-mitochondrial interaction, thereby rescuing mtDNA replication and distribution in DRP1 mutants. Altogether, our results demonstrate that ER sheet-mitochondria contact sites regulate replication and distribution of mtDNA.

Results

Mitobulbs are clusters of mtDNA that fail to disperse

Defects or loss of fission proteins cause the appearance of large nucleoids within bulb-like mitochondrial structures termed mitobulbs (*14-16*), altering nucleoid distribution within mitochondrial networks (*14*). While this indicates an important role of mitochondrial fission in the proper distribution of nucleoids, the underlying mechanism remains unclear.

Mutation or deletion of the mitochondrial fission protein DRP1 causes the formation of mitobulbs that are primarily present in the perinuclear region of the cell (*13-16*). We observed a similar phenotype in primary fibroblasts from patients with a dominant negative mutation in the middle domain of DRP1 which is required for DRP1 oligomerization (*31*) (**Fig. 1A;** mitochondria (TMRM) and nucleoids (picogreen)). Multiple copies of replicating mtDNA observed in individual mitobulbs when labeled with the nucleotide analog EdU (**Fig. 1B-C**). This suggests that mtDNA can actively replicate in mitobulbs but fail to distribute along mitochondrial networks, resulting in a decrease in total nucleoid numbers (*14, 15*). Nevertheless, DRP1 mutants had fewer EdU-positive nucleoids compared to control cells (**Fig. 1D**), suggesting that the loss of DRP1 function affects mtDNA replication. Altogether, our data indicate that mitochondrial fission is essential for proper mtDNA replication and distribution.

Mutation in DRP1 affects ER-mitochondria contact sites

Previous studies have shown that mtDNA replication initiation occurs at sites where mitochondria are in contact with ER tubules and that loss of ER tubules impairs mtDNA replication (*18, 19*). To determine whether fission defects alter mitochondria-ER interaction, we measured ER-mitochondria contact sites in DRP1 mutant primary fibroblasts. We performed a proximity ligation assay (PLA) for Calnexin (general ER marker), and TOM20 (mitochondria) to identify mitochondria-ER contact sites. To assess the specificity of the interaction, we also co-labeled the cells for Calnexin and TOM20. Clear PLA foci were present at sites where Calnexin and TOM20 signals overlapped (**Fig 2A**; IgG control and **Full image in sup. Fig. S1**), indicating the identification of authentic ER-mitochondria contact sites. We observe a significant increase in PLA foci in DRP1 mutants (**Fig 2A-B**), suggesting an increased ER-mitochondria contact sites.

To further validate our PLA data, we measured ER-mitochondria contact sites by transmission electron microscopy (TEM). As mitochondrial fission has been associated with ER tubules (*17-19*) which are generally correlated the with smooth ER as found by TEM (*32-35*), we first quantified the interaction between mitochondria and smooth ER. However, there was no difference in smooth ER-mitochondria contact sites between control and DRP1 mutant fibroblasts (**Fig. 2C-D**). While previous studies have mostly focused on the interaction between mitochondria and smooth ER/ER tubules, mitochondria can also interact with rough ER(*29, 30, 36*). This interaction can in fact readily be observed in control fibroblasts (**Fig 2C**). Importantly, this interaction was further enhanced in DRP1 mutant fibroblasts, as shown by the increase in both the number of ERMCS per mitochondrial length and the length of these ERMCS (**Fig 2C, E**). Extensive interactions between mitochondria and rough ER were also evident in a FIB-SEM analysis of DRP1 mutant fibroblasts (**Fig 2F**). Altogether, our data indicate that ER-mitochondria contact sites

are increased in DRP1 mutants and that this increase is mainly contributed by rough ER-mitochondria contact sites.

A global increase in ER sheets-mitochondrial interaction in DRP1 mutants

Rough ER, as identified by TEM, mostly correlates with ER structures termed ER sheets (*32-35*), which is also supported by our FIB-SEM analysis of rough ER-mitochondria contact sites (**Fig. 2F**). As ER sheets are mostly enriched in the perinuclear area where mitobulbs are also found, we measured the interaction between mitochondria and ER sheets using PLA. For this, we used the ER sheet marker CLIMP63 and the mitochondrial marker TOM20. As shown in **Fig 3A-B**, DRP1 mutants had significantly increased mitochondria-ER sheets interaction compared to control cells. We then validated our observations using super-resolution structured illumination microscopy (SIM) in cells labeled with mitotracker orange (mitochondria) and CLIMP63 (ER sheets) (**Fig 3C**). Consistent with the PLA results, there was an increased colocalization between CLIMP63-labeled ER sheets and mitochondria in DRP1 mutant cells, as quantified using Manders' coefficient (**Fig 3D**). The specificity of the measure was validated by rotating one of the channels 90° before measuring Manders' coefficient (**Fig 3D**). As Manders' coefficients can be affected by structural changes in the organelles tested (*37*), we also measured the overlap between the two structures (see methods) and observed a similar increase in interaction (Fig. 3E). Altogether, our data demonstrate that the interaction between CLIMP63-positive ER sheets and mitochondria is increased in DRP1 mutants.

Differential regulation of ER sheets-mitochondria interaction in DRP1 mutants

ER-mitochondria contact sites are mediated by several protein interaction partners present in the ER and mitochondrial outer membrane. While most of these pairs are expected to be present in both ER tubules and sheets, RRBP1 is an ER sheet-specific protein (*38-40*). To determine if specific ER sheet-mitochondria protein tethers were altered in DRP1 mutant fibroblasts, we performed PLA for RRBP1 and its mitochondrial binding partner SYNJ2BP. In contrast to our TEM and PLA results using general ER (calnexin) and ER sheet (CLIMP63) markers, there were fewer RRBP1-SYNJ2BP contact sites in DRP1 mutants (**Fig. 4A-B**) compared to control cells. To further confirm this result, we imaged mitochondria (mitotracker orange) and ER sheets (RRBP1) by SIM (**Fig. 4C**). Consistent with the PLA data, we observed a significant decrease in the interaction between RRBP1-positive ER sheets and mitochondria as measured by Manders' coefficients and the overlap between the two organelles (**Fig. 4D-E**). Altogether, our data indicate that while DRP1 mutant fibroblasts show an overall increase in ER sheet-mitochondria contact sites, the specific interaction between the ER sheet resident protein RRBP1 and its mitochondrial partner SYNJ2BP is decreased.

ER sheets are associated with mitobulbs in DRP1 mutants

As ER sheets are predominantly present in the perinuclear region of the cell where mitobulbs are also present, we next determined if ER sheets are associated with mitobulbs. To test this, we labeled control and DRP1 mutant fibroblasts for mitochondria (Mitotracker orange), ER sheets (CLIMP63), and ER (RTN4) and imaged them by confocal microscopy. Mitobulbs were present in the perinuclear region associated with ER sheets, but absent from the peripheral region

characterized by RTN4-positive ER tubules (**Fig. S2**). In fact, the vast majority of mitobulbs were closely associated with ER sheets (**Fig. 5A, quantification in B**), supporting the idea that ER sheets interact with mitobulbs. To further confirm the presence of physical interactions between mitobulbs and ER sheets, we performed PLA for CLIMP63 (ER sheets) and TOM20 (mitochondria). PLA foci were visible at sites where ER sheets were in close contact with mitobulbs (**Fig 5C,** quantification in **5D**), consistent with an interaction between the two structures. Similar results were observed when Calnexin was used instead of CLIMP63 for the PLA (**Fig 5D**). Consistent with this, mitobulbs were associated with CLIMP63-positive ER sheets in SIM images (**Fig E**). Altogether, these results indicate that the increase in ER sheet-mitochondria contact sites present in DRP1 mutant fibroblasts is correlated with mitobulb formation.

Mutation or knockdown of DRP1 alters ER sheet structure

As our results indicate that the interaction between mitochondria and ER sheets is altered in DRP1 mutant fibroblasts, we determined whether this could be associated with alterations in ER sheet structure. For this, we immunolabelled control and DRP1 mutant cells for the ER sheets marker CLIMP63 and found that DRP1 mutants had altered ER sheets compared to control cells. These alterations were characterized by a punctate appearance mostly apparent towards the periphery, and sometimes thick patches of sheets in the perinuclear region (**Fig 6A**, an enlarged image showing ER sheet structure; complete cell in **Fig. S2**). The overall area covered by ER sheets was also expanded in DRP1 mutant fibroblasts (**Fig. 6B**). Similar alterations were observed in ER sheets marked with RRBP1 (**Fig. 6C**). Overall, 80% of mutant cells showed an altered ER sheet phenotype (**Fig. 6D**). CLIMP63 and RRBP1-positive ER sheets also had a more punctate appearance when imaged by SIM (Fig. 6E, quantification in F).

To further confirm the structural alteration in ER sheets, we measured the ER area in our TEM imaged (Fig. 2C), where ER sheets were identified as rough ER densely covered with ribosomes. ER sheets from DRP1 mutants had reduced surface area compared to the control (**Fig 6G**), supporting our immunofluorescence data. On the other hand, ER tubule area (identified as smooth ER, free of ribosomes) were similar in control and DRP1 mutants (**Fig 6G**), consistent with the absence of alterations in ER-mitochondria contact sites for these structures (Fig. 2D). Altogether, our data indicate that the structure of ER sheets is altered in DRP1 mutants. Nevertheless, protein levels of CLIMP63, RRBP1, the general ER marker RTN4, Calnexin, and the mitochondrial proteins TOM20 and ATP5a were similar between control and DRP1 mutant cells, indicating that the changes induced by DRP1 mutation are not caused by changes in protein expression levels (**Fig. 6H**).

While our results indicate that loss of DRP1 function alters ER sheet structure, we wanted to eliminate the possibility of secondary effects in the human DRP1 mutants we used. We thus knocked down DRP1 (DRP1 KD) in mouse embryonic fibroblasts (MEFs) (**Fig. S3A**) and labeled them with CLIMP63 (ER sheets). Like patient fibroblasts, DRP1 KD MEFs had mostly punctate ER sheets (**Fig. S3B-C**) that covered an expanded area of the cell (**Fig. S3D**).

Modulation of ER sheets recovers the nucleoid defects present in DRP1 mutants

We then determined whether the altered ER sheet structure present in DRP1 mutant fibroblasts is causing the alterations in ER sheet-mitochondria contact sites observed in the same cells. For this, we modulated ER sheet structure by expressing mCherry-tagged CLIMP63 under conditions that did not overtly alter RTN4-positive ER tubules in control cells (**Fig. S4A**) to avoid nucleoid defects caused by the loss of ER tubules (*19*). Importantly, CLIMP63 expression did not rescue the fused mitochondrial phenotype of the DRP1 mutant (**Fig. S4B**). Nevertheless, CLIMP63 expression altered ER sheet structure resulting in an expanded web-like ER sheet network in both control and DRP1 mutant fibroblasts (**Fig. S5**). Importantly, this was accompanied by a loss of the punctate structures typically observed in mutant cells transfected with mCherry alone (**Fig. S5**), suggesting that CLIMP63 expression can at least partially rescue the ER sheet defects observed in DRP1 mutants. To determine if this was associated with a change in ER sheets-mitochondria interactions, we performed PLA for CLIMP63 (ER sheets) and TOM20 (mitochondria). CLIMP63 expression did not affect mitochondria-ER sheet interaction in control cells (**Fig. 7A**) but rescued the excessive contact sites found in DRP1 mutant cells (**Fig. 7A**). Similarly, the number of mitobulbs associated with PLA foci was reduced in DRP1 mutant cells expressing CLIMP63 (**Fig. 7B**), indicating that recovery of ER sheet structure in DRP1 mutants normalizes its interaction with mitochondria.

Loss of DRP1 results in enlarged nucleoids (**Fig. 1A**) that are likely caused by nucleoid aggregation (*14-16*). To determine the effect of modulating ER sheets on this nucleoid aggregation, we transiently transfected control and DRP1 mutant fibroblasts with mCherry or mCherry-CLIMP63 and immunolabelled them for mitochondria (TOM20) and nucleoids (TFAM). We first determined the effect of the mCherry-CLIMP63 expression on nucleoid aggregation by measuring nucleoid size. Nucleoid size was significantly reduced in DRP1 mutants expressing mCherry-CLIMP63 compared to cells expressing only mCherry (**Fig. 7C-D, Full cell in Fig. S6**), consistent with CLIMP63 expression stimulating nucleoid distribution out of mitobulbs. We then reasoned that if CLIMP63 rescues nucleoid distribution, it should also rescue the decreased nucleoid numbers present in DRP1 mutant cells (*14*). Indeed, while mCherry-CLIMP63 expression did not significantly affect nucleoid numbers in control cells, it caused a significant increase in overall nucleoid content in DRP1 mutants (**Fig 7E**). Altogether, these results indicate that modulating ER sheet structure rescues nucleoid aggregation in DRP1 mutants. As the enlarged nucleoids present in DRP1 mutant cells are found within mitobulbs, we also determined the effect of the mCherry-CLIMP63 expression on the presence of mitobulbs. While almost all mitobulbs present in mCherry-transfected DRP1 mutant fibroblasts contained TFAM-positive nucleoids, mCherry-CLIMP63 expression drastically reduced this number (**Fig. 7F**). On the other hand, the total number of enlarged, bulb-like mitochondrial structures was unchanged (**Fig. 7G**), suggesting that DRP1 is still required to maintain mitochondrial structure in these conditions. Altogether, our data indicate that nucleoid segregation is regulated by ER sheet-mitochondria interaction independently of DRP1-dependent fission.

Altering ER sheets in DRP1 mutant promotes mtDNA replication and distribution

While our results are consistent with CLIMP63 expression promoting nucleoid distribution away from mitobulbs, it remained possible that it also rescued mtDNA replication. Thus, we measured

the effect of CLIMP63 expression on mtDNA replication. Replicating DNA was labeled with EdU, after which cells were directly fixed, immunolabelled for mitochondria (TOM20), and imaged by confocal microscopy. In cells expressing mCherry, DRP1 mutants had fewer EdU- positive nucleoids compared to control cells (Fig. 7H), suggesting that DRP1 is required for proper mtDNA replication. Importantly, the expression of CLIMP63 rescued the number of EdU foci in DRP1 mutant cells (Fig. 7H), suggesting that the effect of DRP1 on nucleoid replication is the consequence of altered ER sheet-mitochondria interaction. On the other hand, CLIMP63 expression did not significantly alter the number of EdU foci in control cells (Fig. 7H), indicating that modulating ER sheet structure does not directly affect mtDNA replication.

As clusters of EdU-positive mtDNA are found within mitobulbs (**Fig. 1B-C**), we then specifically addressed the effect of CLIMP63 expression on mtDNA replication within mitobulbs. Consistent with the total EdU counts, expression of CLIMP63 in DRP1 mutant fibroblasts caused a large increase in EdU incorporation in mtDNA present within mitobulbs (**Fig. 7I**). We then took advantage of the accumulation of EdU foci within mitobulbs to determine whether the reduction in nucleoid size that we observed in CLIMP63-transfected DRP1 mutant cells (**Fig. 7D**) is due to the rescue of nucleoid segregation from mitobulbs towards the rest of the mitochondrial network. To do that, we chased EdU for 24 hours before fixing the cells. Consistent with our observation that the number of nucleoid-containing mitobulbs was decreased in CLIMP63-expressing cells (**Fig. 7F**), the number of EdU-positive mitobulbs was decreased in CLIMP63-expressing DRP1 mutant cells, but not mCherry-expressing cells at 24 hours (**Fig. 7I**). Importantly, this was not due to the loss of overall EdU staining in mutant cells (**Fig. 7J**). Overall, our data indicate that modulating ER sheets-mitochondrial interaction through altering ER sheet structure reactivates both mtDNA replication and nucleoid distribution in DRP1 mutant cells even in the absence of mitochondrial fission. Thus, proper ER sheets- mitochondria interaction is essential to modulate mtDNA replication and nucleoid segregation.

Discussion

mtDNA replication is associated with mitochondrial dynamics, especially mitochondrial fusion which is required for mtDNA replication and integrity (*11, 12*). On the other hand, mitochondrial fission has been suggested to be associated with nucleoid segregation based on the fact that defects in mitochondrial fission result in nucleoid aggregation within mitobulbs (*13, 15, 16*). With the help of Mitomate Tracker, an automated tool developed in our lab, we have shown that this alters overall nucleoid distribution within mitochondrial networks (*14*). Nevertheless, the mechanism by which nucleoid distribution is altered in cells with fission defects remain unclear. Here, we demonstrate that ER sheet-mitochondria contact sites regulate mtDNA replication and distribution within mitochondrial networks.

ER tubule-mitochondria contact sites play an important role in regulating mitochondrial dynamics and function (*17, 18, 39*) including mtDNA replication (*19*). Our data shows that ER sheets also regulate mtDNA replication and segregation by directly interacting with mitochondria. This is consistent with the previous observation that ER sheets interact with mitochondria and regulate lipid metabolism in mouse liver cells (*29*), suggesting an important physiological role for this interaction. As we previously showed that, in DRP1 mutants, nucleoids aggregate around the perinuclear region where ER sheets are found (*14*), we further defined how ER sheets-mitochondria interaction impacts this process. Our data demonstrates that cells with defective DRP1 have altered ER sheet structure. Furthermore, DRP1 mutant cells showed increased interaction between ER sheets and mitochondria, including with mitobulbs. Of note, we did not observe distinct changes in ER tubules in our cell models, possibly because ER tubular formation requires the variable domain of DRP1 (*41*) which is still intact in our mutant lines (mutation in the middle domain (G362D))(*31*). Overall, these results indicate that DRP1-defective cells have altered ER sheet-mitochondria contact sites.

The altered ER sheet-mitochondria contact sites present in DRP1 mutant cells was associated with the accumulation of mtDNA within mitobulbs. Importantly modulating ER sheets by expressing CLIMP63 rescued ER sheet-mitochondria contact sites, nucleoid aggregation, and nucleoid number in DRP1 mutants, supporting the idea that ER sheets-mitochondria contact sites regulate nucleoid distribution. In addition, our EdU data demonstrated that proper ER sheet ERMCS is necessary to actively regulate mtDNA replication. Altogether, our data show that ER sheet-mitochondria contact sites are essential for both mtDNA replication and distribution, and that this occurs independently of DRP1-dependent mitochondrial fission.

While we demonstrated that ER sheets-mitochondria contact sites play an important role in mtDNA replication and distribution, ER tubules are still required. This was shown in a previous study overexpressing CLIMP63 under conditions that caused the complete loss of ER tubules, which significantly reduced mitochondrial DNA replication in cells with wild-type DRP1 (*19*). However, when we expressed CLIMP63 under conditions that do not affect tubular ER structure, mtDNA replication was unaltered in cells with wild-type DRP1. Furthermore, ER tubule structure and interaction with mitochondria were unaffected in cells with defective DRP1. This further suggests that the regulation of mtDNA replication and segregation by ER sheets is independent of ER tubules.

Our study also provides novel insights into the defects present in DRP1 mutant patients. Reported human DRP1 mutations are mostly found in the middle and GTPase domains of DRP1, leading to peripheral neuropathy, epilepsy, optic atrophy, and encephalopathy in these patients (*31, 42*). Here, we have used patient fibroblasts with a dominant negative mutation in the middle domain of DRP1 (G362D), leading to refractory epilepsy(*31*). At the cellular level, conditional deletion of DRP1 in mice affects the movement of mitochondria to the nerve terminal, leading to the loss of dopamine neurons (*43*), while its postnatal deletion in CA1 hippocampal neurons results in functionally impaired mitochondria at the nerve terminals (*44*). Based on our key findings here, we speculate that the altered mtDNA replication and nucleoid distribution could severely hamper the movement of functional mitochondria towards the synaptic nerve terminal in the patient neurons and thereby impairing neuronal signaling. Further research work is required to validate this hypothesis in neuronal cells.

Altogether, our results demonstrate the importance of ER sheets-mitochondria contact sites in mtDNA maintenance and nucleoid distribution. Alteration of these contact sites following DRP1 mutation leads the perinuclear accumulation of mtDNA, which could explain the defects observed in these cells in the absence of overt metabolic alterations (*31*).

Materials and Methods

Reagents

Cell culture reagents were obtained from Wisent. Other chemicals were purchased from Sigma-Aldrich, except where indicated.

Cell culture and live cell imaging

Primary human fibroblasts (controls and DRP1 mutants) were generated from skin biopsies, collected as part of an approved research protocol (Research Ethics Board of the Children's Hospital of Eastern Ontario (DRP1 mutants)), and written informed consent from participants was obtained. This study was performed in accordance with the Declaration of Helsinki. Biopsy samples were processed as described and cultured in Dulbecco's modified Eagle's medium (DMEM) containing 10% fetal bovine serum (FBS), supplemented with Penicillin/Streptomycin (100 IU/ml/100µL/mL)(*31*). Immortalized Mouse Embryonic Fibroblasts (MEFs) were cultured in DMEM supplemented with 10% fetal bovine serum. For live cell imaging, cells were seeded onto glass bottom dishes and allowed to adhere to the plate. Then cells were stained for 30 minutes with 250 nM TMRM (Thermo fisher Scientific, T668) and the DNA dye PicoGreen (Thermo Fisher Scientific, P11495) (3 µL/mL). After staining, cells were washed 3 times with pre-warmed 1X phosphate buffered saline (PBS), and normal growth media was added prior to imaging.

siRNA treatment

MEFs were seeded onto 24 well dish and transfected with 15nM of DRP1 siRNA (Thermo Fisher Scientific, Silencer Select, 4390771) and negative siRNA (Thermo Fisher Scientific, Silencer Select, 4390843) using siLenFect lipid reagent (Bio-Rad,1703361). After 48 hrs, cells were treated again with siRNA for another 48 hours. The cells were collected for either western blotting or seeded onto the coverslips for immunofluorescence.

Transient transfection of primary cells

Primary cells were trypsinized and centrifuged at 577 X g for 10 minutes. Cell pellets were suspended in 10µl of the Neon transfection buffer R (ThermoFisher Scientific, MPK1096). Cells were transiently transfected with mCherry (gift from Michael Davidson, Addgene, 54517), mCherry-tagged CLIMP63 (gift from Gia Voeltz (*45*), Addgene, 136293), DRP1-GFP (gift from Thomas Cribbs (*46*))using the Neon transfection system (ThermoFisher Scientific, MPK5000) according to the manufacturer's protocol. To minimize effects on ER tubules, minimal concentrations (1µg) of mCherry and mCherry-CLIMP63 plasmids were used.

Immunofluorescence

Cells were seeded onto glass coverslips (Fisherbrand, 1254580) and allowed to adhere overnight. Mitochondria was stained using 50 nM Mitotracker Orange (Thermo fisher scientific, M7510) prior to fixing for certain experiment. Cells were fixed with 4% paraformaldehyde for 15 minutes

at room temperature (RT). For antigen retrieval, cells were incubated in sodium citrate buffer (pH 6.0) for 10 minutes at 95°C. Then, cells were permeabilized with 1% BSA / 0.2% Triton X-100 in PBS followed by blocking with 1% BSA / 0.1% Triton X-100 in PBS. The following antibodies were used: CLIMP63 (Rb, Abcam, ab84712, 1:150), CLIMP63 (Mo, ENZO, ENZ-ABS669, 1: 200), RRBP1 (Rb, Novus Biologicals, NBP1-32813, 1:200), , TOM20 (Rb, Abcam, ab186735, 1:250), mtTFAM (Mo, Novusbio, NBP1-71648, 1:150), Calnexin (Mo, Millipore, MABF2067, 1:200), RTN4/NOGOA (Rb, Bio-Rad, AHP1799, 1:200), ATP5a (Mo, Abcam, ab14748, 1:150), SYNJ2BP (Rb, Sigma-Aldrich, HPA000866, 1:200), RRBP1 (Mo, Thermo Fisher Scientific, MA5-18302, 1:200). Next, cells were incubated with fluorescent tagged secondary antibody (Jackson Immunoresearch, 1:500).

Microscopy

Images were acquired with a Leica TSC SP8 confocal microscope fitted with a 63x/1.40 oil objective using the optimal resolution for the wavelength (determined using the Leica software). For super-resolution microscopy, z-stack images were taken using a Zeiss Elyra 7.2 lattice structured illumination microscopy (SIM) fitted with 63X/ 1X (CLIMP63, mitotracker labeled images) or 1.5X (RRBP1, mitotracker labelled images) oil objective and dual sCMOS cameras (pco.edge). CLIMP63 and RRBP1 images with a spatial resolution of 90 nm were constructed using the SIM^2 processing, using a iteration strength appropriate for the signal to noise ratio (3-5) for the CLIMP63 or RRB1 data. Mitotracker images were processed using standard SIM.

Image analysis

All image manipulation and analysis were done in Image J/Fiji except where noted. To verify the interaction between organelles (bulb-like mitochondria and ER sheets), line scan analysis was performed using the *RGB profiler* in Image J. To avoid bias during manually classification of ER structure, images were renamed to random numbers and both control and mutant images were shuffled together. The blindfolded ER sheet images were manually classified as structured or altered using reference images. In addition, we segmented the ER sheet images in ImageJ (Filter/minimum (0.5), Filter/Median (1.0), then thresholding and adjusting the resulting image using Binary/Erode) and measured total area ER sheets using the Analyse Particle function. Mitochondrial structures were manually quantified by binning them into the indicated categories (short, intermediate, elongated). For the SIM images, the processed images were used to measure ER sheet-mitochondria contact sites using Manders' colocalization coefficient. Maximum z-projected images were used for the analysis. ER sheets were segmented using Image J *filters* (median (1), mean (25)) and thresholded by default method. Mitochondria were segmented using the Image J tool *Tubeness* and thresholded by default method (*14*). Segmented images were analyzed using the Image J plugin *Just another colocalization plugin (JaCoP)*(*47*). ER sheet-mitochondria contact site area was measured by identifying regions of colocalization in the SIM processed images using the Image J tool *Hue*. The average ER sheet size was measured using

segmented ER sheets images using the Image J tool *Analyze particle*. 3D-SIM reconstructions were performed using Bitplane Imaris software v. 9.5.

Proximity Ligation Assay (PLA)

Cells were grown on glass coverslips and fixed with 4% paraformaldehyde. Following antigen retrieval, cells were permeabilized with 1% BSA/0.2% Triton X-100 in PBS for 15 minutes at RT. The ER was marked with an antibody recognizing CLIMP63 or calnexin or RRBP1 and mitochondria was marked with an antibody recognizing TOM20 or SYNJ2BP. The PLA assays were performed using Duolink In Situ green kit Mouse/ Rabbit (Sigma Aldrich) following the manufacturer's protocol. The primary antibodies were then labelled using fluorescent-tagged secondary antibodies. Total and mitobulb associated PLA foci were manually counted at the site of CLIMP63-TOM20 and RRBP1-SYNJ2BP signal while overall calnexin-TOM20 foci were quantified using the *analyze particles* function in ImageJ.

Transmission Electron Microscopy (TEM)

Primary fibroblasts were seeded on Nunc Lab-Tek chamber slides (Thermo Fisher Scientific, 177437) and allowed to adhere overnight. Cells were washed with 0.1M sodium cacodylate buffer (pH 7.3) and fixed with 2.5% glutaraldehyde in 0.1M sodium cacodylate buffer (pH 7.3), overnight at 4°C. Fixed cells were further processed in McGill's facility for electron microscopy research (FEMR). Images were acquired using a EMS208S electron microscope (Philips) by an independent trained operator in University of Quebec in Trois-Rivières' TEM facility. We manually measured ER surface area for 10 randomly chosen rough ER/smooth ER in each of the four quadrants per image of the cell. Rough ER-mitochondrial contact sites in the perinuclear region were manual quantified, considering only contact sites ≤ 30 nm based on a previous study (*48*). Smooth ER-mitochondria contact sites were manually measured near the cellular periphery per image of the cell.

Focused Ion Beam Scanning Electron Microscopy (FIB-SEM)

Sample blocks for analysis by FIB-SEM were prepared as for TEM. Each Epon block was trimmed and mounted on a 45° pre-titled SEM stub and coated with a 4-nm thick of Pt to enhance electrical conductivity. Milling of serial sections and imaging of block face after each Z-slice was carried out with the Helios Nanolab 660 DualBeam using Auto Slice & View 4.1 software (FEI Company, Hillsboro, OR USA).

A block was first imaged to determine the orientation relationship between the block face of ion and electron beams. A protective Pt layer 26.3 µm long, 1.5 µm wide and 2 µm thick was deposited on the surface of the region of interest to protect the resin volume from ion beam damaging and correct for stage and/or specimen drift, i.e., perpendicular to the image face of the volume to be milled. Trenches on both sides of the region were created to minimize re-deposition during the automated milling and imaging. Distinct imaging fiducials were generated for both ion beam and electron beam imaging and were used to dynamically correct for any drift in x and y during a run

by applying appropriate SEM beam shifts. Milling was performed at 30 kV with an ion beam current of 2.5 nA, stage tilt of -0.5 degree, working distance of 4 mm. With each step, 4 nm thickness of the material was removed with the ion beam. Each newly milled block face was imaged with Through the Lens Detector (TLD) for backscattered electrons at an accelerating voltage of 2 kV, beam current of 0.4 nA, stage tilt of 37.5 degree, and working distance of 2 mm. The pixel resolution was 4.15 nm with a dwell time of 30 µs. Pixel dimensions of the recorded image were 1536 x 1024 pixels. 201 images were collected, and the contrast of the images inversed.

Processing of FIB-SEM images

Three-dimensional reconstruction of one long mitochondrion and associated ER network was done with the Dragonfy sofware (Ver. 2022.1; Object Research Systems, Montreal QC). Mitochondria and ER from DRP1 mutant patient cells were segmented manually within the painting tool in Dragonfy from 75 slices as 4 nm slice spacing throw 0.3 µm depth. The boolean operation option was used to highlight the intersection regions between mitochondria and ER (contact site regions). The total number of voxels segmented as RE was 8 513 191, 2 337 756 voxels as mitochondria and 56 677 as contact sites between the two organelles.

Western Blot

Cells were lysed in 10 mM Tris-HCl, pH 7.4, 1mM EDTA, 150 mM NaCl, 1% Triton X-100, 50 mM sodium fluoride, complemented with a protease inhibitor cocktail (Sigma-Aldrich), centrifuged at 15890 X g for 5 minutes and protein supernatants collected. Protein concentrations were estimated calorimetrically by DC protein assay kit (BioRad). For SDS-PAGE, 20 µg (siRNA treatment in MEFs)/25 µg (Mitochondrial and ER proteins in human fibroblasts) of proteins were mixed with 1X Lammeli buffer containing β-mercaptoethanol, then subjected to SDS-PAGE, transferred to nitrocellulose membranes and blotted with the indicated antibodies (DRP1 (BD Transduction Laboratories, 611112, 1:1000), CLIMP63 (Mo, ENZO, ENZ-ABS669, 1: 500), TOM20 (Rb, Abcam, ab186735, 1:1000), Calnexin (Mo, Millipore, MABF2067, 1:1000), RTN4/NOGOA (Rb, Bio-Rad, AHP1799, 1:1000), ATP5a (Mo, Abcam, ab14748, 1:1000), HRP-tagged Actin (1:10,000). Membranes were then incubated with a 1:5000 dilution of horseradish peroxidase-conjugated secondary antibodies (Jackson Immunoresearch) and visualized by enhanced chemiluminescence (Thermo Fisher scientific) using a Bio-Rad imaging system.

EdU Labeling

Primary fibroblasts (Control and DRP1 mutants) were incubated with 60µM EdU for 2 hours at 37°C. For the chase experiments, the EdU containing media was replaced with fresh media and incubated further for 24 hours. Cells were then fixed with 4% paraformaldehyde for 15 minutes at RT, permeabilized and EdU detected using Click-iT EdU imaging kit (Thermo Fisher Scientific,

C10337). Cells were then immunolabelled for TOM20 (Abcam, ab186735, 1:250). EdU foci in mitobulbs and total EdU foci were manually counted.

Data analysis and statistics

All graphs and statistical analysis were done using R. Immunofluorescence data were quantified and images representative of at least three independent experiments shown (exact n are in the quantification figures). Data are represented as average ± SD as specified in figure legends. Statistical significance was determined using Student's t test (between 2 groups) or one-way ANOVA with a tukey post hoc test (multiple comparisons).

Acknowledgements

This work was supported by grants from the Natural Sciences and Engineering Research Council of Canada and the Fondation de l'UQTR to MG and the Canadian Foundation for Innovation to JV. HSI was supported by a Queen Elizabeth II Diamond Jubilee Scholarship and an FRQ-NT scholarship. Object Research Systems provided access to Dragonfly software.

Author contribution

HSI performed the cell biology experiments. HSI and MG designed the experiments. HSI, JDG, SB and MG analysed the data. AL reconstructed 3D FIB-SEM data with direction from FR. KAN performed SIM imaging with direction from JV. MAL provided the clinical samples. HSI and MG wrote the paper. All authors reviewed and discussed the manuscript.

References

1. J. B. Spinelli, M. C. Haigis, The multifaceted contributions of mitochondria to cellular metabolism. *Nature Cell Biology* **20**, 745-754 (2018).
2. F. J. Bock, S. W. G. Tait, Mitochondria as multifaceted regulators of cell death. *Nature Reviews Molecular Cell Biology* **21**, 85-100 (2019).
3. C. Giorgi, S. Marchi, P. Pinton, The machineries, regulation and cellular functions of mitochondrial calcium. *Nature Reviews Molecular Cell Biology* **19**, 713-730 (2018).
4. Gerald S. Shadel, Tamas L. Horvath, Mitochondrial ROS Signaling in Organismal Homeostasis. *Cell* **163**, 560-569 (2015).
5. P. Lisowski, P. Kannan, B. Mlody, A. Prigione, Mitochondria and the dynamic control of stem cell homeostasis. *EMBO reports* **19**, (2018).
6. V. Tiku, M.-W. Tan, I. Dikic, Mitochondrial Functions in Infection and Immunity. *Trends in Cell Biology* **30**, 263-275 (2020).
7. H. Otera *et al.*, Mff is an essential factor for mitochondrial recruitment of Drp1 during mitochondrial fission in mammalian cells. *Journal of Cell Biology* **191**, 1141-1158 (2010).
8. O. C. Losón, Z. Song, H. Chen, D. C. Chan, D. D. Newmeyer, Fis1, Mff, MiD49, and MiD51 mediate Drp1 recruitment in mitochondrial fission. *Molecular Biology of the Cell* **24**, 659-667 (2013).
9. H. Chen *et al.*, Mitofusins Mfn1 and Mfn2 coordinately regulate mitochondrial fusion and are essential for embryonic development. *Journal of Cell Biology* **160**, 189-200 (2003).
10. S. Cipolat, O. M. de Brito, B. Dal Zilio, L. Scorrano, OPA1 requires mitofusin 1 to promote mitochondrial fusion. *Proceedings of the National Academy of Sciences* **101**, 15927-15932 (2004).
11. E. Silva Ramos *et al.*, Mitochondrial fusion is required for regulation of mitochondrial DNA replication. *PLOS Genetics* **15**, (2019).
12. H. Chen *et al.*, Mitochondrial Fusion Is Required for mtDNA Stability in Skeletal Muscle and Tolerance of mtDNA Mutations. *Cell* **141**, 280-289 (2010).
13. R. Ban-Ishihara, T. Ishihara, N. Sasaki, K. Mihara, N. Ishihara, Dynamics of nucleoid structure regulated by mitochondrial fission contributes to cristae reformation and release of cytochrome c. *Proceedings of the National Academy of Sciences* **110**, 11863-11868 (2013).
14. H. S. Ilamathi *et al.*, A new automated tool to quantify nucleoid distribution within mitochondrial networks. *Scientific reports* **11**, 22755 (2021).
15. T. Ishihara *et al.*, Dynamics of Mitochondrial DNA Nucleoids Regulated by Mitochondrial Fission Is Essential for Maintenance of Homogeneously Active Mitochondria during Neonatal Heart Development. *Molecular and Cellular Biology* **35**, 211-223 (2015).
16. N. Ishihara, T. Ishihara, A. Ota, Mitochondrial nucleoid morphology and respiratory function are altered in Drp1-deficient HeLa cells. *The Journal of Biochemistry* **167**, 287-294 (2020).
17. R. G. Abrisch, S. C. Gumbin, B. T. Wisniewski, L. L. Lackner, G. K. Voeltz, Fission and fusion machineries converge at ER contact sites to regulate mitochondrial morphology. *Journal of Cell Biology* **219**, (2020).
18. J. R. Friedman *et al.*, ER Tubules Mark Sites of Mitochondrial Division. *Science* **334**, 358-362 (2011).
19. S. C. Lewis, L. F. Uchiyama, J. Nunnari, ER-mitochondria contacts couple mtDNA synthesis with mitochondrial division in human cells. *Science* **353**, (2016).
20. J. R. Friedman, G. K. Voeltz, The ER in 3D: a multifunctional dynamic membrane network. *Trends in Cell Biology* **21**, 709-717 (2011).
21. D. S. Schwarz, M. D. Blower, The endoplasmic reticulum: structure, function and response to cellular signaling. *Cellular and Molecular Life Sciences* **73**, 79-94 (2015).

22. Y. Shibata *et al.*, Mechanisms Determining the Morphology of the Peripheral ER. *Cell* **143**, 774-788 (2010).
23. H. Zhang, J. Hu, Shaping the Endoplasmic Reticulum into a Social Network. *Trends in Cell Biology* **26**, 934-943 (2016).
24. J. Rieusset, The role of endoplasmic reticulum-mitochondria contact sites in the control of glucose homeostasis: an update. *Cell Death & Disease* **9**, (2018).
25. M. Hamasaki *et al.*, Autophagosomes form at ER–mitochondria contact sites. *Nature* **495**, 389-393 (2013).
26. S. Böckler, B. Westermann, Mitochondrial ER Contacts Are Crucial for Mitophagy in Yeast. *Developmental Cell* **28**, 450-458 (2014).
27. R. Rizzuto *et al.*, Close Contacts with the Endoplasmic Reticulum as Determinants of Mitochondrial Ca 2+ Responses. *Science* **280**, 1763-1766 (1998).
28. A. A. Rowland, G. K. Voeltz, Endoplasmic reticulum–mitochondria contacts: function of the junction. *Nature Reviews Molecular Cell Biology* **13**, 607-615 (2012).
29. I. Anastasia *et al.*, Mitochondria-rough-ER contacts in the liver regulate systemic lipid homeostasis. *Cell Reports* **34**, (2021).
30. N. Ilacqua *et al.*, A three-organelle complex made by wrappER contacts with peroxisomes and mitochondria responds to liver lipid flux changes. *Journal of Cell Science* **135**, (2022).
31. J. R. Vanstone *et al.*, DNM1L-related mitochondrial fission defect presenting as refractory epilepsy. *European Journal of Human Genetics* **24**, 1084-1088 (2015).
32. M. West, N. Zurek, A. Hoenger, G. K. Voeltz, A 3D analysis of yeast ER structure reveals how ER domains are organized by membrane curvature. *Journal of Cell Biology* **193**, 333-346 (2011).
33. Y. Shibata, G. K. Voeltz, T. A. Rapoport, Rough Sheets and Smooth Tubules. *Cell* **126**, 435-439 (2006).
34. M. Puhka *et al.*, Progressive sheet-to-tubule transformation is a general mechanism for endoplasmic reticulum partitioning in dividing mammalian cells. *Molecular Biology of the Cell* **23**, 2424-2432 (2012).
35. M. Puhka, H. Vihinen, M. Joensuu, E. Jokitalo, Endoplasmic reticulum remains continuous and undergoes sheet-to-tubule transformation during cell division in mammalian cells. *Journal of Cell Biology* **179**, 895-909 (2007).
36. T. Harada *et al.*, Palmitoylated CKAP4 regulates mitochondrial functions through an interaction with VDAC2 at ER–mitochondria contact sites. *Journal of Cell Science*, (2020).
37. R. Filadi *et al.*, Mitofusin 2 ablation increases endoplasmic reticulum–mitochondria coupling. *Proceedings of the National Academy of Sciences* **112**, (2015).
38. V. Hung *et al.*, Proteomic mapping of cytosol-facing outer mitochondrial and ER membranes in living human cells by proximity biotinylation. *eLife* **6**, (2017).
39. S. Aoyama-Ishiwatari, Y. Hirabayashi, Endoplasmic Reticulum–Mitochondria Contact Sites—Emerging Intracellular Signaling Hubs. *Frontiers in Cell and Developmental Biology* **9**, (2021).
40. E. L. Wilson, E. Metzakopian, ER-mitochondria contact sites in neurodegeneration: genetic screening approaches to investigate novel disease mechanisms. *Cell Death & Differentiation* **28**, 1804-1821 (2020).
41. Y. Adachi *et al.*, Drp1 Tubulates the ER in a GTPase-Independent Manner. *Molecular Cell* **80**, 621-632.e626 (2020).
42. R. Banerjee, A. Mukherjee, S. Nagotu, Mitochondrial dynamics and its impact on human health and diseases: inside the DRP1 blackbox. *Journal of Molecular Medicine*, (2021).
43. A. Berthet *et al.*, Loss of Mitochondrial Fission Depletes Axonal Mitochondria in Midbrain Dopamine Neurons. *Journal of Neuroscience* **34**, 14304-14317 (2014).

44. L. Y. Shields *et al.*, Dynamin-related protein 1 is required for normal mitochondrial bioenergetic and synaptic function in CA1 hippocampal neurons. *Cell Death & Disease* **6**, e1725-e1725 (2015).
45. Y. Shibata *et al.*, The reticulon and DP1/Yop1p proteins form immobile oligomers in the tubular endoplasmic reticulum. *The Journal of biological chemistry* **283**, 18892-18904 (2008).
46. S. Strack, J. T. Cribbs, Allosteric Modulation of Drp1 Mechanoenzyme Assembly and Mitochondrial Fission by the Variable Domain. *Journal of Biological Chemistry* **287**, 10990-11001 (2012).
47. S. Bolte, F. P. Cordelieres, A guided tour into subcellular colocalization analysis in light microscopy. *Journal of microscopy* **224**, 213-232 (2006).
48. G. r. Csordás *et al.*, Structural and functional features and significance of the physical linkage between ER and mitochondria. *Journal of Cell Biology* **174**, 915-921 (2006).

Figure Legends

Figure 1. Multiple mtDNA copies accumulate within mitobulbs in DRP1 mutant fibroblasts. (A) Representative live cell images showing the mitochondrial marker TMRM (magenta) and picogreen-stained DNA (green) in control and DRP1 mutant human fibroblasts. The zoomed images show the enlarged nucleoids present in mitobulbs (arrowheads). (B) Representative images of mCherry-expressing DRP1 mutants labeled for EdU (green) and TOM20 (mitochondria, magenta). Arrowheads indicate EdU-positive mtDNA in mitobulbs. Scale bar 10μm. (C) Quantification of number of EdU foci/mitobulb. Each point represents an individual cell, with 45 cells quantified in 3 independent experiments. Bars show the average ± SD. (D) Quantification of EdU foci in control and DRP1 mutants cells labelled with EdU for 4 hours. Each point represents one cell, with at least 44 cells quantified in 3 independent experiments. Bars show the average ± SD. *** $p<0.001$ two-sided t-test.

Figure 2. Increased contact sites between rough ER and mitochondria in DRP1 mutant fibroblasts. (A) Representative images of control and DRP1 mutant fibroblasts showing the PLA for Calnexin and TOM20 (white), along with Calnexin (ER, green), and TOM20 (mitochondria, magenta). Arrowheads denote PLA foci on mitobulbs. Scale bar 2 μm. (B) Quantification of Calnexin-TOM20 PLA. Each data point represents one cell. Bars represent the average of 40 cells per genotype in 3 independent experiments ± SD ** $p<0.01$ two-sided t-test (C) Representative TEM images of control and DRP1 mutant fibroblasts. Arrowheads denote ER-mitochondria contact sites. Scale bar 1 μm. (D) Quantification of the ERMCs length (μm) per mitochondrial perimeter (Left) and number of ERMCS per mitochondrial perimeter (Right) in TEM images of smooth ER. Each data point represents one cell. Bars represent the average of 15 cells per genotype ± SD. (E) Quantification of the ERMCs length (μm) per mitochondrial perimeter (Left) and number of ERMCS per mitochondrial perimeter (Right) in TEM images of rough ER. Each data point represents one cell. Bars represent the average of 15 cells per genotype ± SD * $p<0.05$, ** $p<0.01$ two-sided t-test. (F) FIB-SEM images of a DRP1 mutant mitochondria showing its association with rough ER. Left, FIB-SEM image, middle and right, 3D reconstruction. Scale bar 500 nm.

Figure 3. Increased contact sites between CLIMP63-labelled ER and mitochondria in DRP1 mutant fibroblasts. (A) Representative images of control and DRP1 mutant fibroblasts showing the PLA for CLIMP63 and TOM20 (White), along with CLIMP63 (ER sheets, green), TOM20 (mitochondria, magenta) and nuclei (Hoechst, blue). Scale bar 10 μm. (B) Quantification of CLIMP63-TOM20 PLA. Each data point represents one cell. Bars represent the average of 50 control and 48 mutant cells in 3 independent experiments ± SD *** $p<0.001$ two-sided t-test. (C) Representative SIM images of control and DRP1 mutant fibroblasts stained for CLIMP63 (ER sheets, green) and Mitotracker orange (mitochondria, magenta) (D) Manders' coefficients calculated from the SIM images in (C). Left, M1 (relative to mitochondria); Right, M2 (relative to the ER). In the turned condition, the CLIMP63 images were rotated 90° to represent a random distribution. Each data point represents one cell. Bars represent the average of 11 cells per genotype ± SD * $p<0.05$ One-way ANOVA (E) Fraction of overlapping signal between ER and mitochondria normalized to mitochondria (Left) or the ER area (Right) in SIM images (C). Each data point represents one cell. Bars represent the average of 11 cells per genotype ± SD * $p<0.05$ two-sided t-test.

Figure 4. Decreased RRPB1-SYNJ2BP contact sites in DRP1 mutant fibroblasts. (A) Representative images of control and DRP1 mutant fibroblasts showing the PLA for RRBP1 and SYNJ2BP (White), along with RRBP1 (ER sheets, green) and SYNJ2BP (mitochondria, magenta). Scale bar 10 µm. (B) Quantification of RRBP1-SYNJ2BP PLA. Each data point represents one cell. Bars represent the average of 50 control and 48 mutant cells in 3 independent experiments ± SD *** $p<0.001$ two-sided t-test. (C) representative SIM images of control and DRP1 mutant fibroblasts stained for RRBP1 (ER sheets, green) and Mitotracker orange (mitochondria, magenta) (D) Manders' coefficients calculated from the SIM images in (C). Left, M1 (relative to mitochondria); Right, M2 (relative to the ER). In the turned condition, the RRBP1 images were rotated 90° to represent a random distribution. Each data point represents one cell. Bars represent the average of 11 cells per genotype ± SD * $p<0.05$ One-way ANOVA (E) Fraction of overlapping signal between ER and mitochondria normalized to mitochondria (Left) or the ER area (Right) in SIM images (C). Each data point represents one cell. Bars represent the average of 11 cells per genotype ± SD * $p<0.05$ two-sided t-test.

Figure 5. ER sheets are associated with mitobulbs. (A-B) Colocalisation between ER sheets and mitobulbs. Colocalisation was measured in cells immunolabelled for CLIMP63 (ER sheets, red) and ATP5a (mitochondria, green). (A) representative image (Top) and Line scan analysis (Bottom) along the line shown in the image. (B) Quantification of the percent of mitobulbs that are associated with CLIMP63-positive ER sheets in two independent DRP1 mutant lines (P1 and P2). Each data point represents one cell. Bars represent the average of 45 control and 45 mutant mitochondria ± SD. (C-D) Interaction between ER sheets and mitobulbs as measured by PLA for TOM20 and CLIMP63 or Calnexin. (C) Representative image of TOM20-CLIMP63 PLA. Arrowheads denote PLA foci (White) on mitobulbs (TOM20, Green) at sites where they contact ER sheets (CLIMP63, Red). (D) Quantification of mitobulbs associated with PLA foci for TOM20-CLIMP63 and TOM20-Calnexin. Each data point represents one cell. Bars represent the average of 48 (CLIMP63 PLA) and 40 cells (Calnexin PLA) in 3 independent experiments ± SD. Scale bars 2 µm. (E) Representative image of 3D rendering of a SIM image (middle, right) showing a mitobulb (magenta) in association with ER sheets (green) in a DRP1 mutant cell, original image on the left. Contact sites (golden yellow) as identified by the Imaris software. The asterisk denotes a mitobulb.

Figure 6. Altered ER sheet structure in DRP1 mutants. (A) Representative images of CLIMP63 staining in control and DRP1 mutant fibroblasts. The white lines denote the edge of the cell as determined by DIC. Full image in **Fig. S2**. Scale bars 10 µm. (B) Quantification of total area covered by ER sheets. Each data point represents one cell. Bars represent the average of 41 cells in 3 independent experiments ± SD *** $p<0.001$ two-sided t-test. (C) Representative images of RRBP1 staining in control and DRP1 mutant fibroblasts. The white lines denote the edge of the cell as determined by DIC. Scale bars 10 µm. (D) Quantification of ER sheet structure as Structured (Blue) or Altered (red; presence of punctate structures and thick ER sheet patches). Each point represents one independent experiment, with at least 20 cells quantified per experiment. Bars show the average ± SD. * $p<0.05$, ** $p<0.01$ One-way ANOVA using the data for Structured ER. (E) Representative SIM images of CLIMP63 (Top) or RRBP1 (Bottom)- labelled ER sheets in Control and DRP1 mutant fibroblasts. (F) Quantification of the average size of individual CLIMP63-labeled (right), RRBP1-labeled (left) ER sheets from SIM images in (E). Each data

point represents one cell. Bars represent the average of 15 cells in 3 independent experiments ± SD *** p<0.001 two-sided t-test. (G) Quantification of the average ER sheet (Left) and ER tubule (Right) area in EM images (Fig. 2C). Each data point represents one cell. Bars represent the average of 10 cells ± SD ** p<0.01 two-sided t-test. (H) WB showing ER (CLIMP63, RTN4, RRBP1, calnexin) and mitochondrial proteins (TOM20, ATP5a) in control and DRP1 mutant human fibroblasts.

Figure 7. CLIMP63 expression rescues nucleoid distribution in DRP1 mutant fibroblasts. (A-B) Quantification of PLA foci (CLIMP63-TOM20) in mCherry and mCherrry-CLIMP63 expressing control and DRP1 mutant cells. Total PLA foci (A) and mitobulbs associated with PLA foci (B) were quantified. Each point represents one cell, with at least 43 cells quantified per condition in 3 independent experiments. Bars show the average ± SD. ** p<0.01, *** p<0.001, ns not significant. One-way ANOVA (C) Representative images of mCherry and mCherrry-CLIMP63 expressing control and DRP1 mutant cells stained for the mitochondrial marker TOM20 (mitochondria, magenta) and the nucleoid marker TFAM (nucleoids, Green). Scale bar 10 µm. (D) Quantification of nucleoid area in mCherry and mCherry-CLIMP63 expressing control and DRP1 mutants from images in **Fig. S6**. Each point represents one cell, with at least 32 cells quantified per condition in 3 independent experiments. Bars show the average ± SD. *** p<0.001, ns not significant. One-way ANOVA. (E-F) Rescue of nucleoid numbers in CLIMP63-expressing DRP1 mutant cells. Quantification of total nucleoids (TFAM-positive, E), mitobulbs containing nucleoids (TFAM-positive, F) and mitochondrial bulb-like structures (independently of the presence of nucleoids, G) in mCherry and mCherrry-CLIMP63 expressing control and DRP1 mutant cells. Each point represents one cell, with 40 mCherry (mch) and 47 mCherry-CLIMP63 cells quantified in 3 independent experiments. Bars show the average ± SD. One way ANOVA (E), two-sided t-test (F, G). * p<0.05, *** p<0.001, ns, not significant. (H) Quantification of EdU foci in control and DRP1 mutants expressing mCherry or mCherry-CLIMP63 in cells labelled with EdU for 4 hours. Each point represents one cell, with at least 43 cells quantified in 3 independent experiments. Bars show the average ± SD. One way ANOVA. * p<0.05, *** p<0.001, ns not significant. (I) Quantification of EdU-positive mitobulbs in EdU-labelled DRP1 mutants expressing mCherry or mCherry-CLIMP63. Cells were pulsed with EdU as in (C) then the EdU was chased for 24 hours where indicated. Each point represents one cell, with at least 44 cells quantified in 3 independent experiments. Bars show the average ± SD. One way ANOVA. *** p<0.001. (J) EdU foci ratio (chase/no chase) from the experiments in (H-I). Each point represents an independent experiment (n=3). Bars show the average ± SD. Two-sided t-test. ns not significant.

Supplementary Figure 1. Calnexin-TOM20 PLA. (A) Representative image of PLA (IgG and TOM20; white) for the antibody control (IgG), along with IgG (red), TOM20 (mitochondria, green) and nuclei (Hoechst, Blue) in control fibroblasts. (B) Representative images of control and DRP1 mutant fibroblasts showing the PLA for Calnexin and TOM20 (white), along with Calnexin (ER, green), TOM20 (mitochondria, magenta) and nuclei (Hoechst, Blue). Scale bar 10 µm.

Supplementary Figure 2. ER structure in DRP1 mutant fibroblasts. Representative images of control (Top) and DRP1 mutant (Bottom) human fibroblasts showing CLIMP63 (ER sheets, Red), RTN4 (ER, Green) and mitochondria (Mitotracker orange, Blue). The enlarged boxed areas show ER structure in the perinuclear area (CLIMP63-positive) and periphery of the cells. Scale bar 10

µm, 2 µm for the enlarged images. Arrowheads denote the localisation of mitobulbs within CLIMP63-positive perinuclear area.

Supplementary Figure 3. ER Structure alterations following DRP1 knockdown in MEFs. (A) WB showing DRP1 expression in WT MEFs transfected with a control siRNA (siCtrl) or a siRNA against DRP1 (siDRP1). (B) Representative images showing CLIMP63 staining in MEFs transfected with control and DRP1 siRNAs. White lines represent the cell edge. Scale bar 10 µm (C) Quantification of ER sheet structure as Structured (Blue) or Altered (red; presence of punctate structures and thick ER sheet patches). Each point represents one independent experiment, with at least 20 cells quantified per experiment. Bars show the average ± SD. * $p<0.05$, Two-sided t-test using the data for Structured ER. (D) Quantification of ER sheet surface area relative to the total cell area (determined by DIC). Each data point represents one cell. Bars represent the average of 54 cells in 3 independent experiments ± SD. ** $p<0.01$ two-sided t-test.

Supplementary Figure 4. ER tubules are not affected by CLIMP63 expression. (A) Representative images of Control cells expressing mCherry and mCherry-CLIMP63 (Magenta) and immunolabelled for RTN4 (ER, green). Scale bar 10 µm, 2 µm for the zoomed images. (B) Quantification of mitochondrial phenotypes (short (green), intermediate (red), elongated/hyperfused (blue)) in mCherry and mCherry-CLIMP63 expressing control and DRP1 mutant fibroblasts. Each point represents an independent experiment. Bars show the average ± SD. Two-way ANOVA. *** $p<0.001$, ns not significant.

Supplementary Figure 5. CLIMP63 expression alters ER sheet structure in control and DRP1 mutants. Representative images of control and DRP1 mutant fibroblasts expressing mCherry or mCherry-CLIMP63 (Magenta) and immunolabelled for CLIMP63 (ER sheets, green). Scale bar 10 µm.

Supplementary Figure 6. CLIMP63 expression rescues nucleoid aggregation in DRP1 mutants. Representative images of control and DRP1 mutant fibroblasts expressing mCherry or mCherry-CLIMP63 (blue) immunolabeled for TFAM (nucleoids, Green) and TOM20 (mitochondria, Magenta). Scale bar 10 µm.

Figure 1

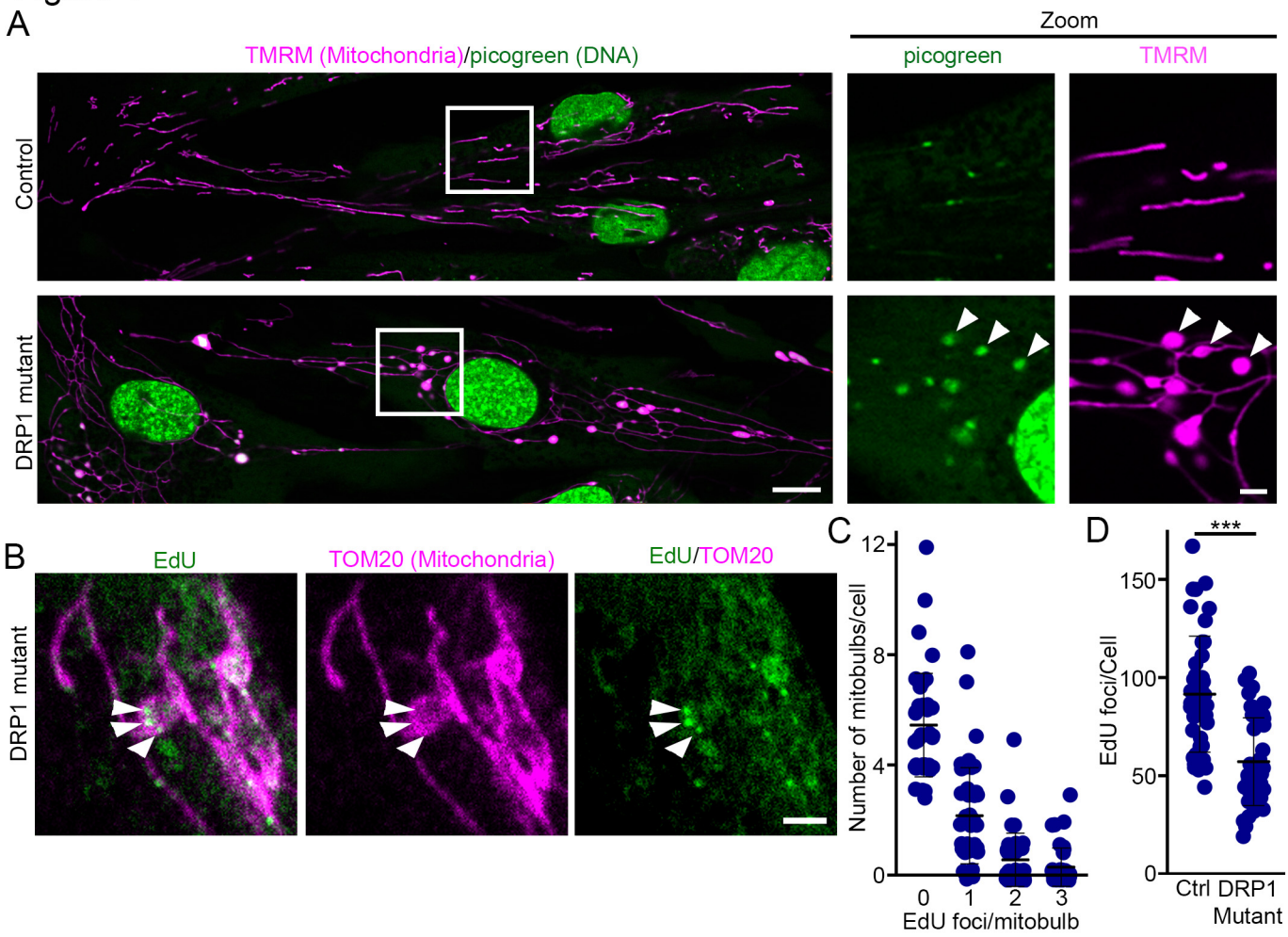

Figure 2

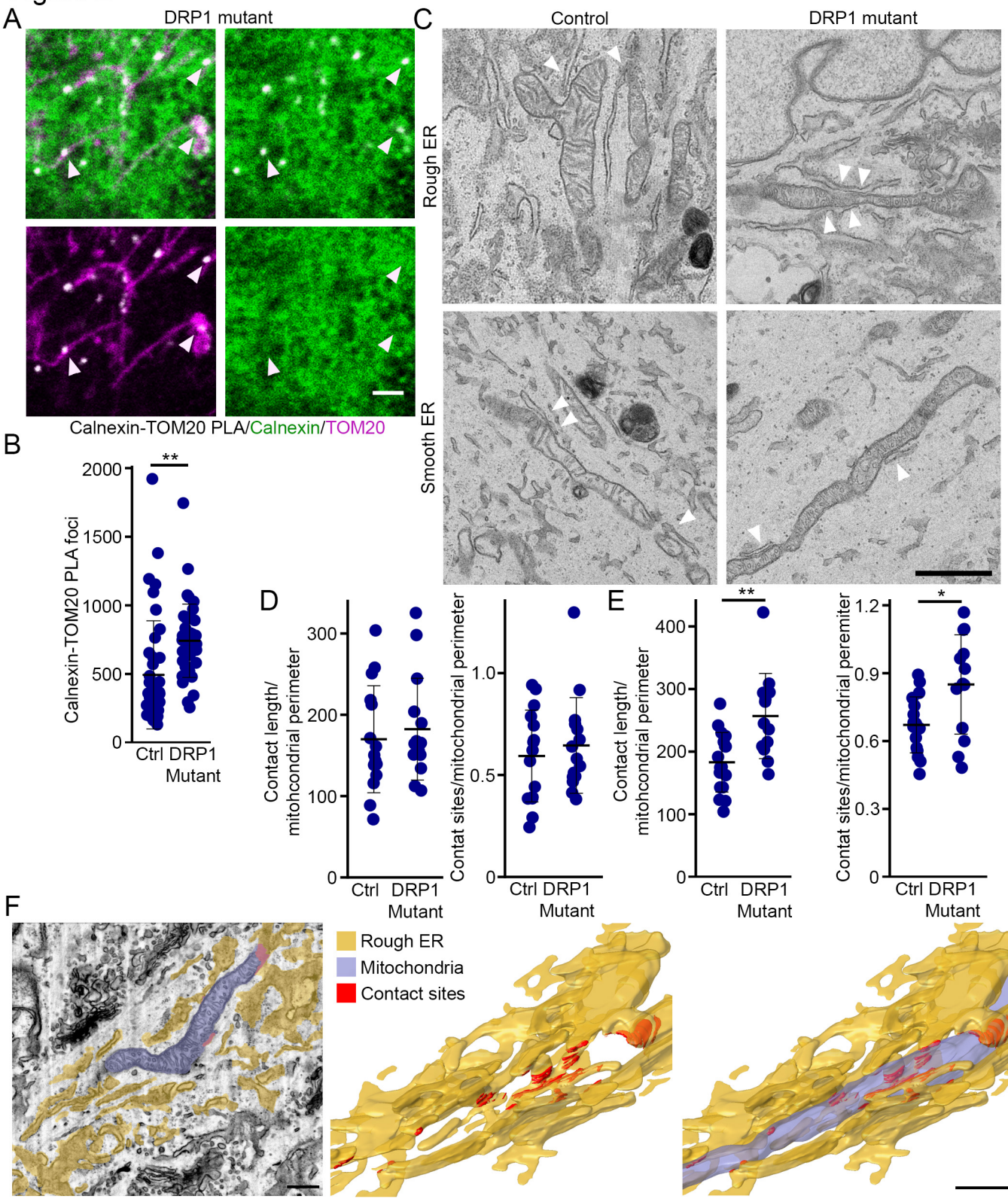

Figure 3

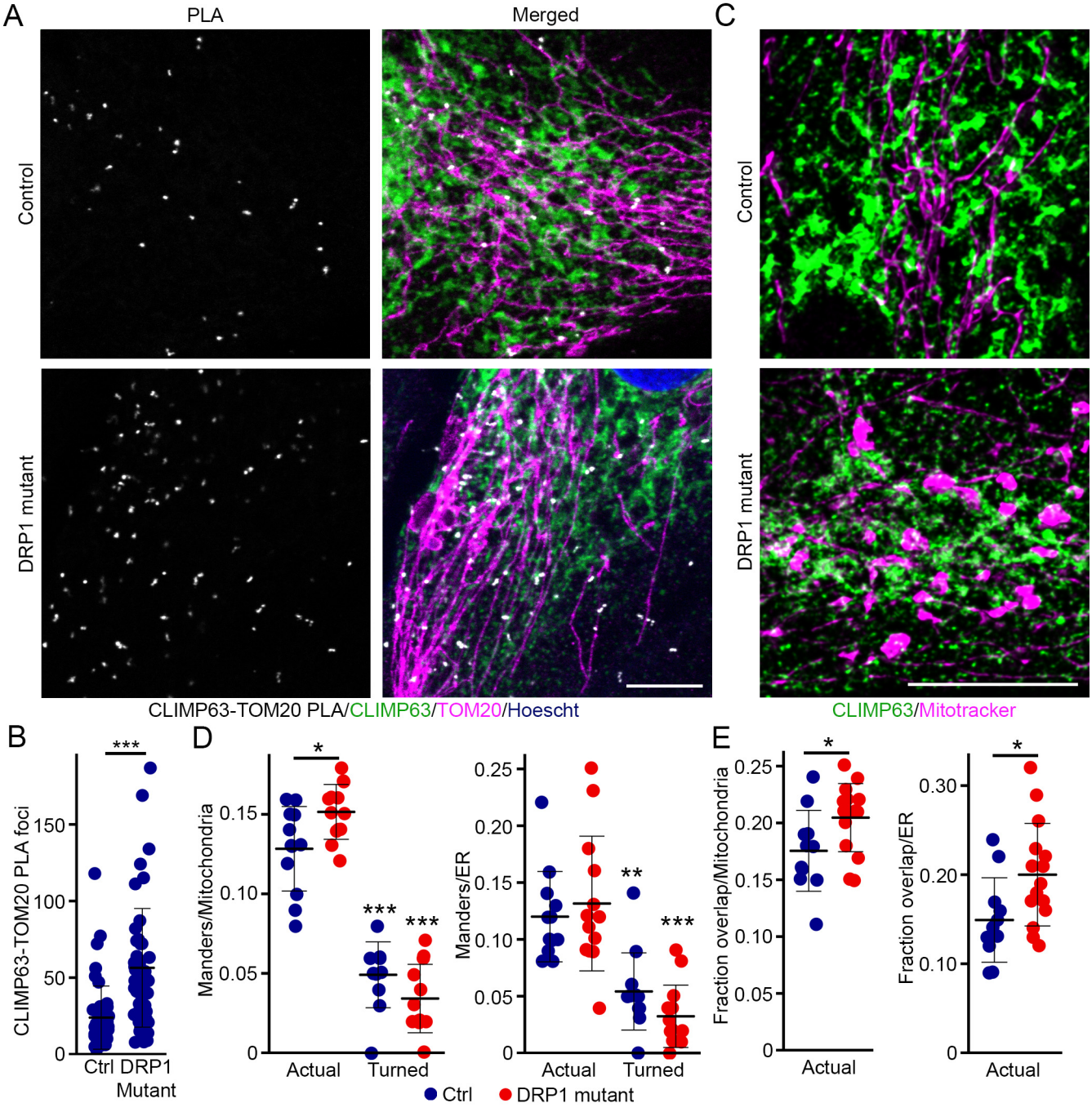

Figure 4

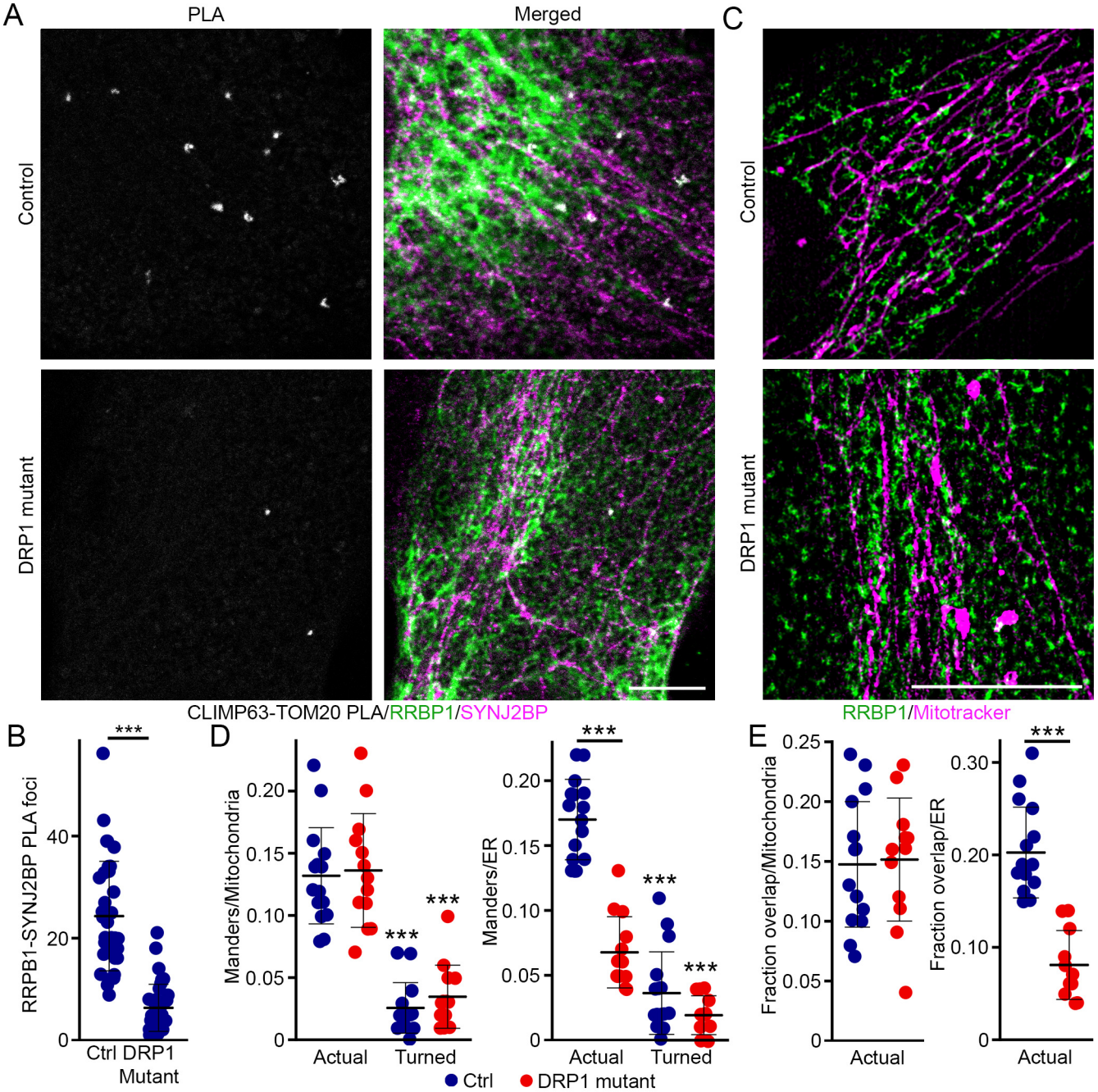

Figure 5

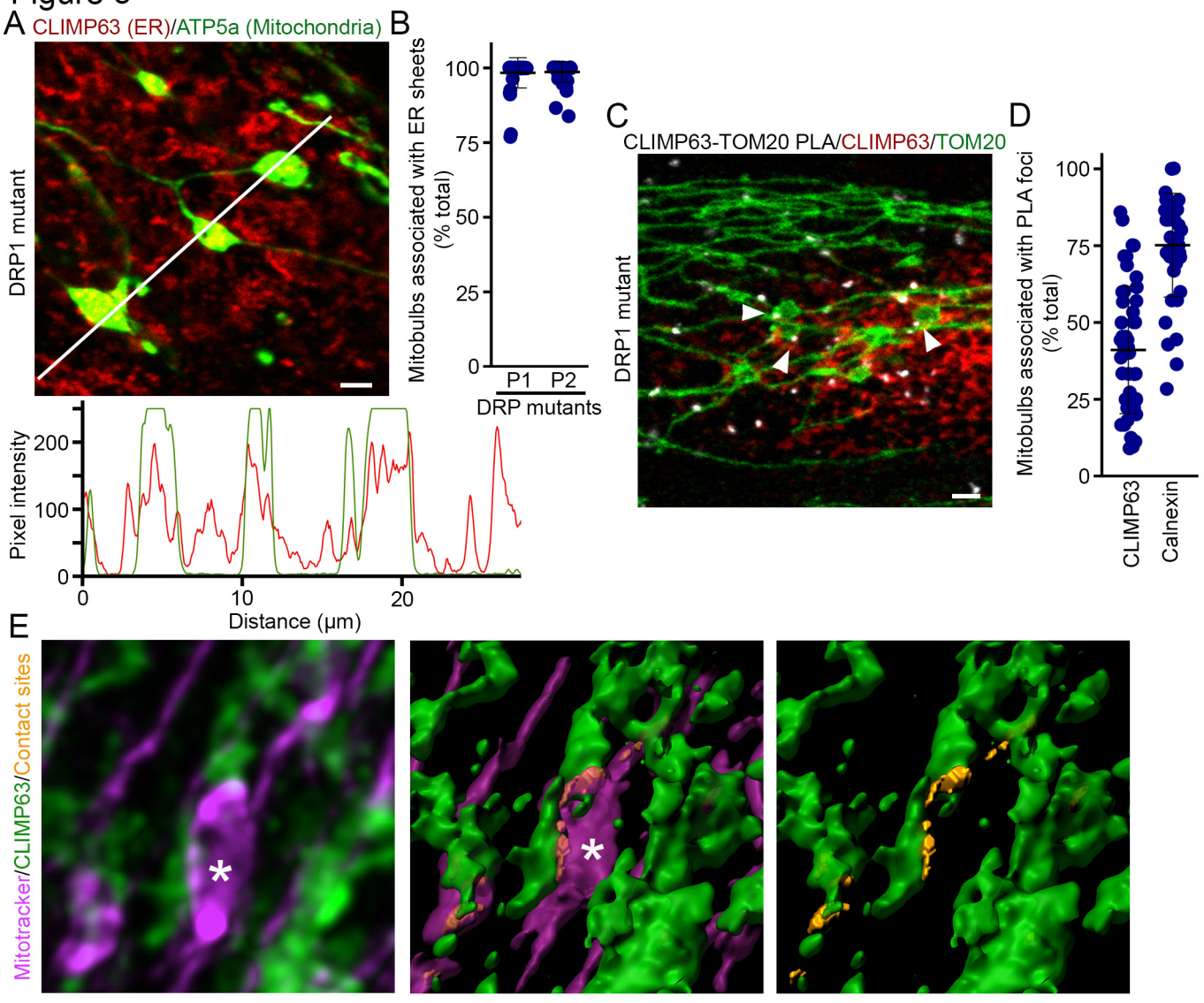

Figure 6

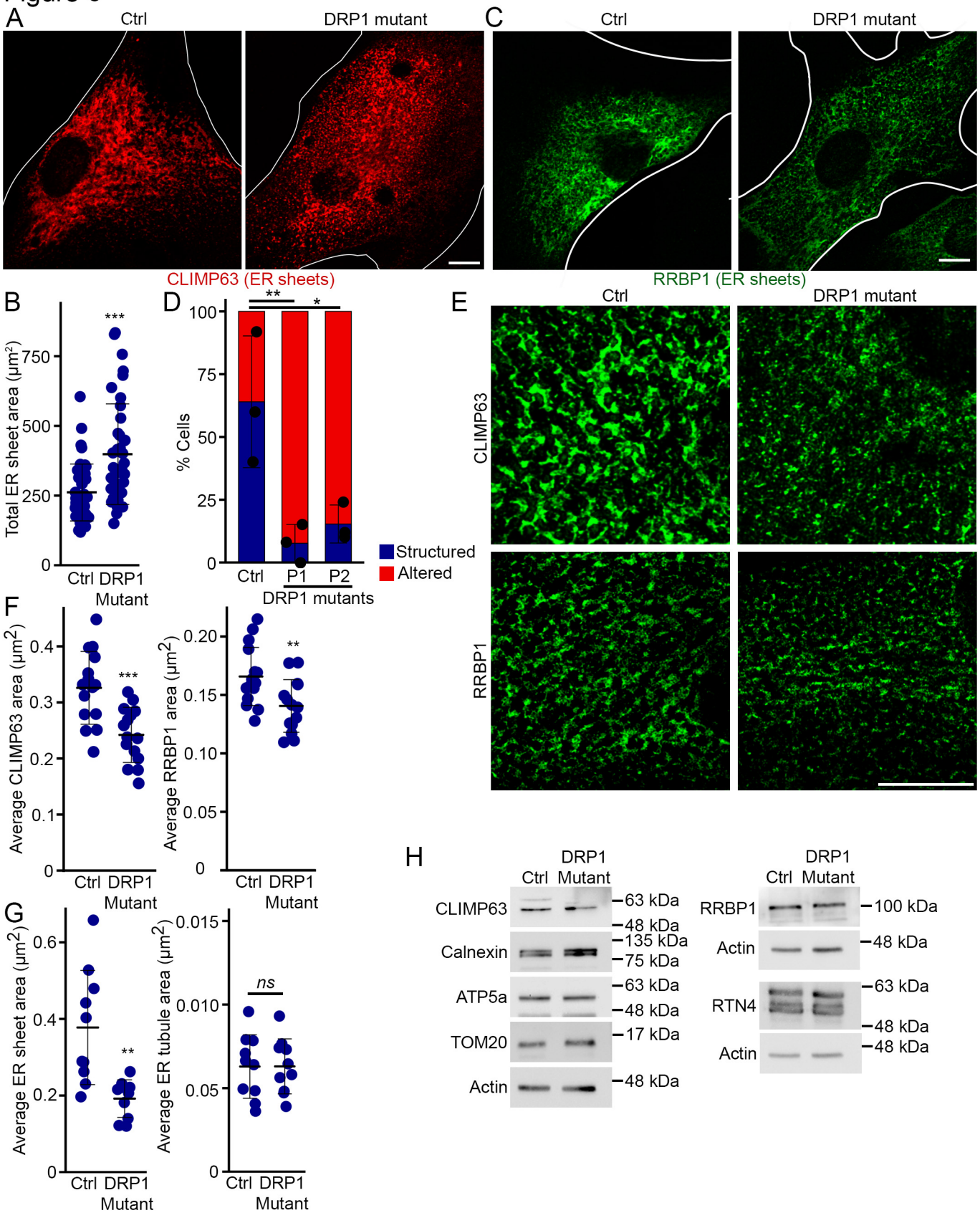

Figure 7

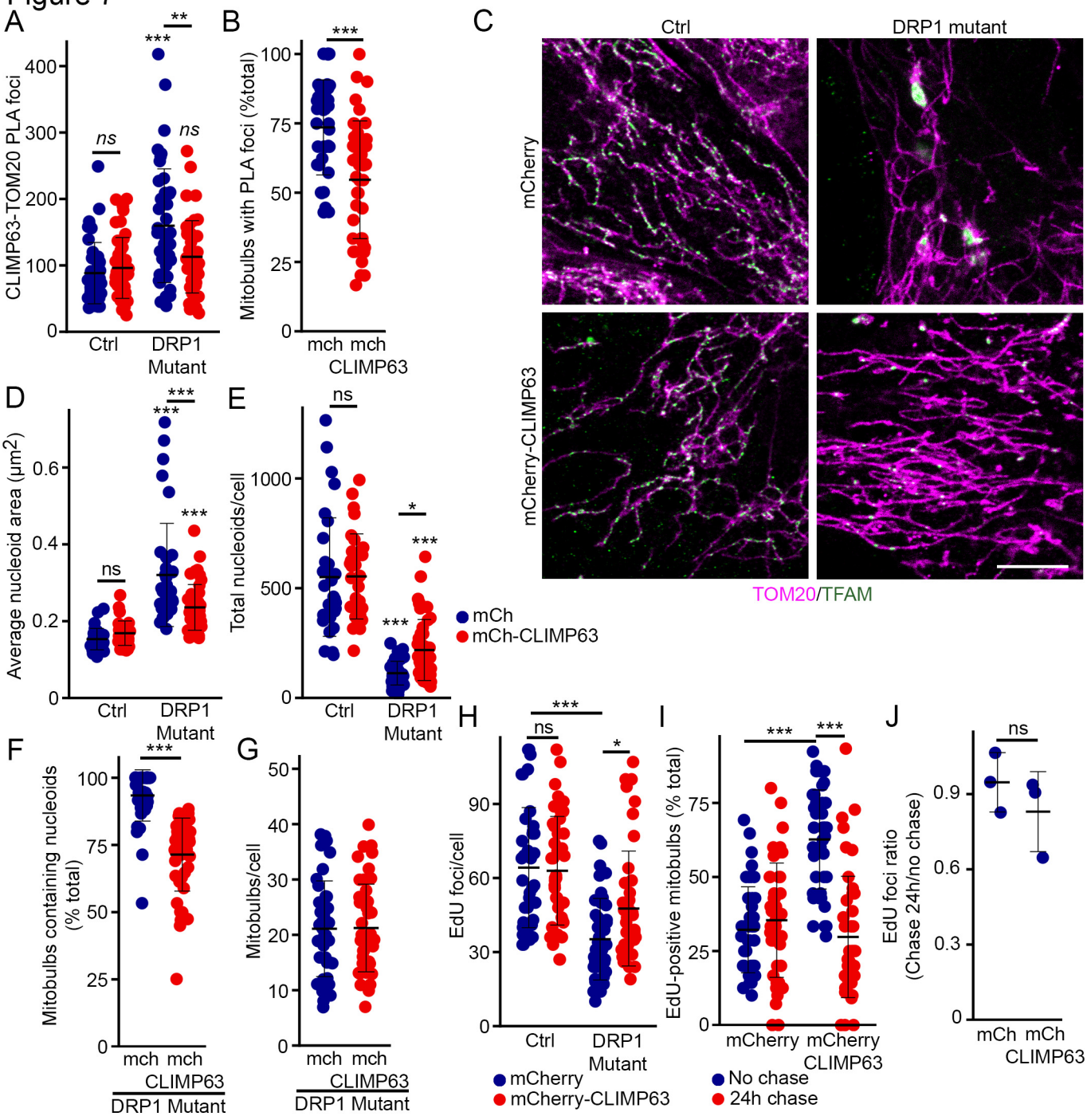

Supplementary Figure 1

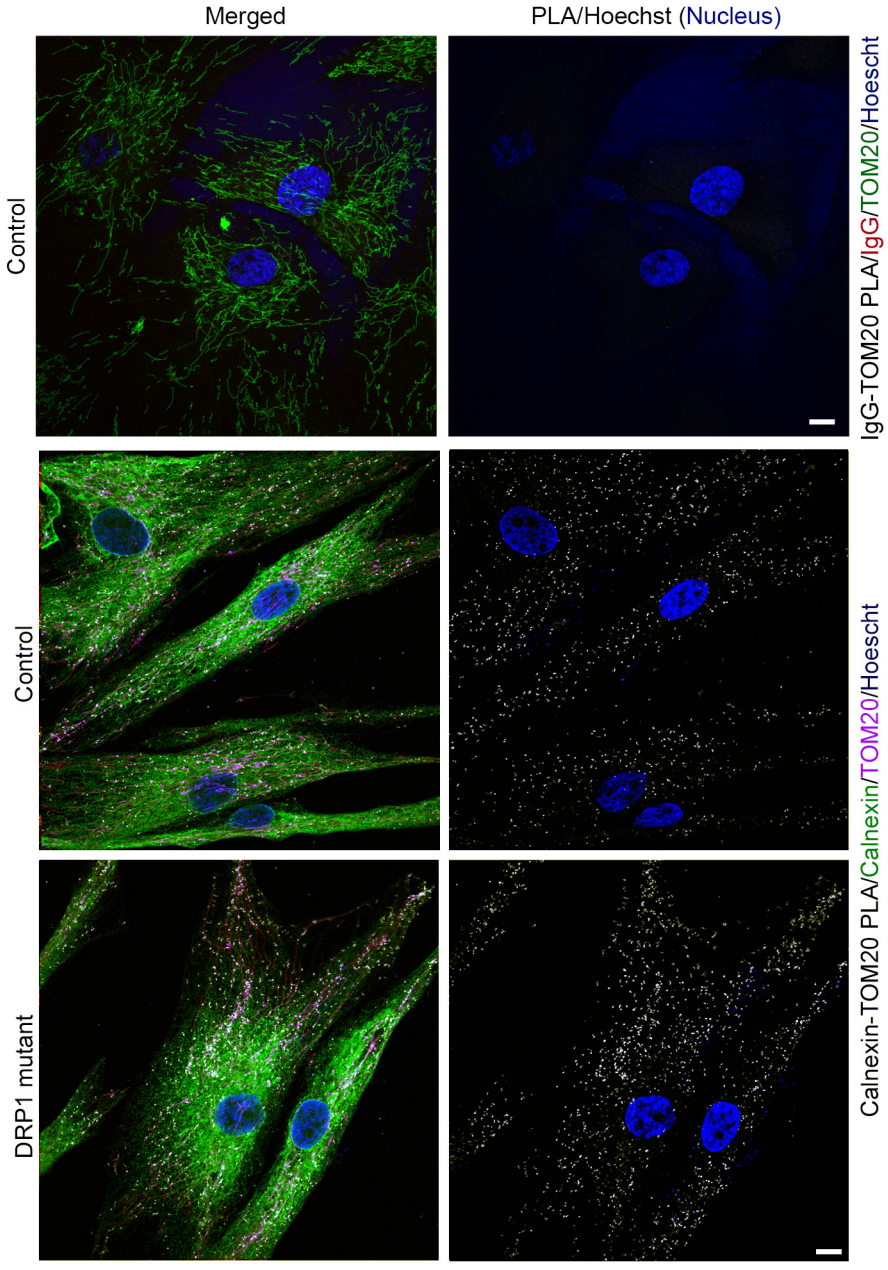

Sup. Figure 2

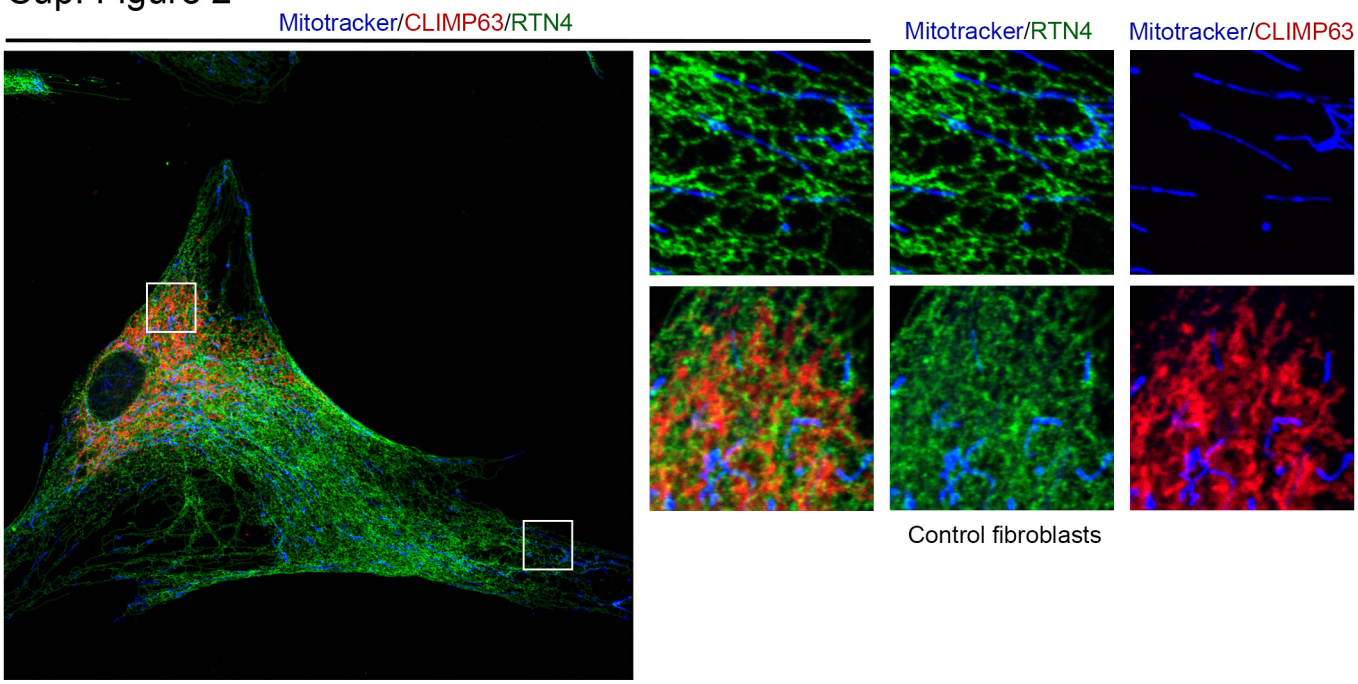

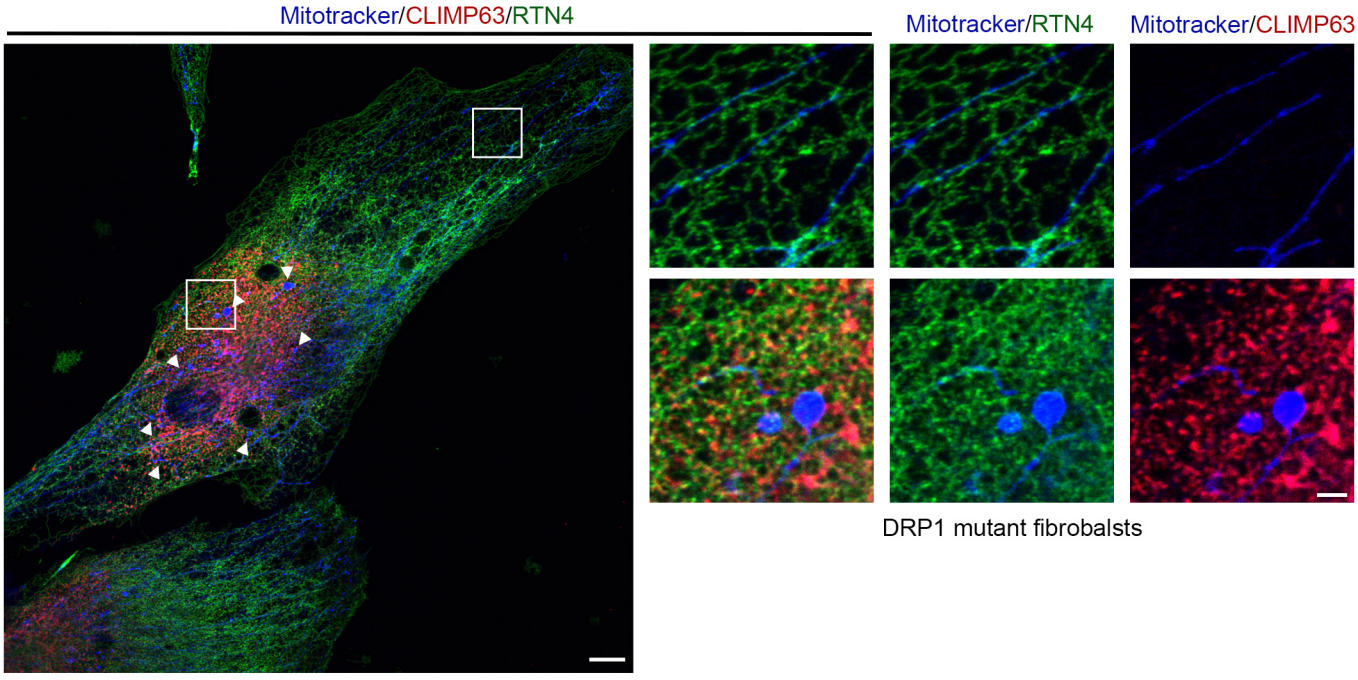

Supplementary Figure 3

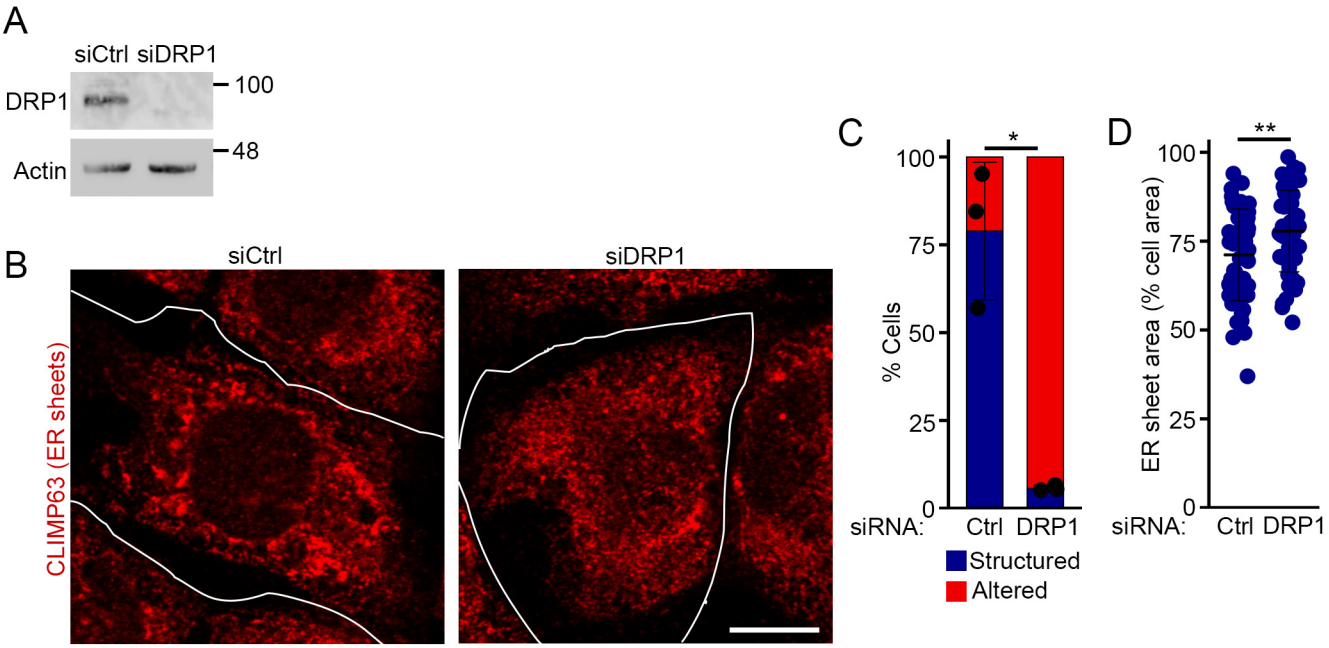

Sup. Figure 4

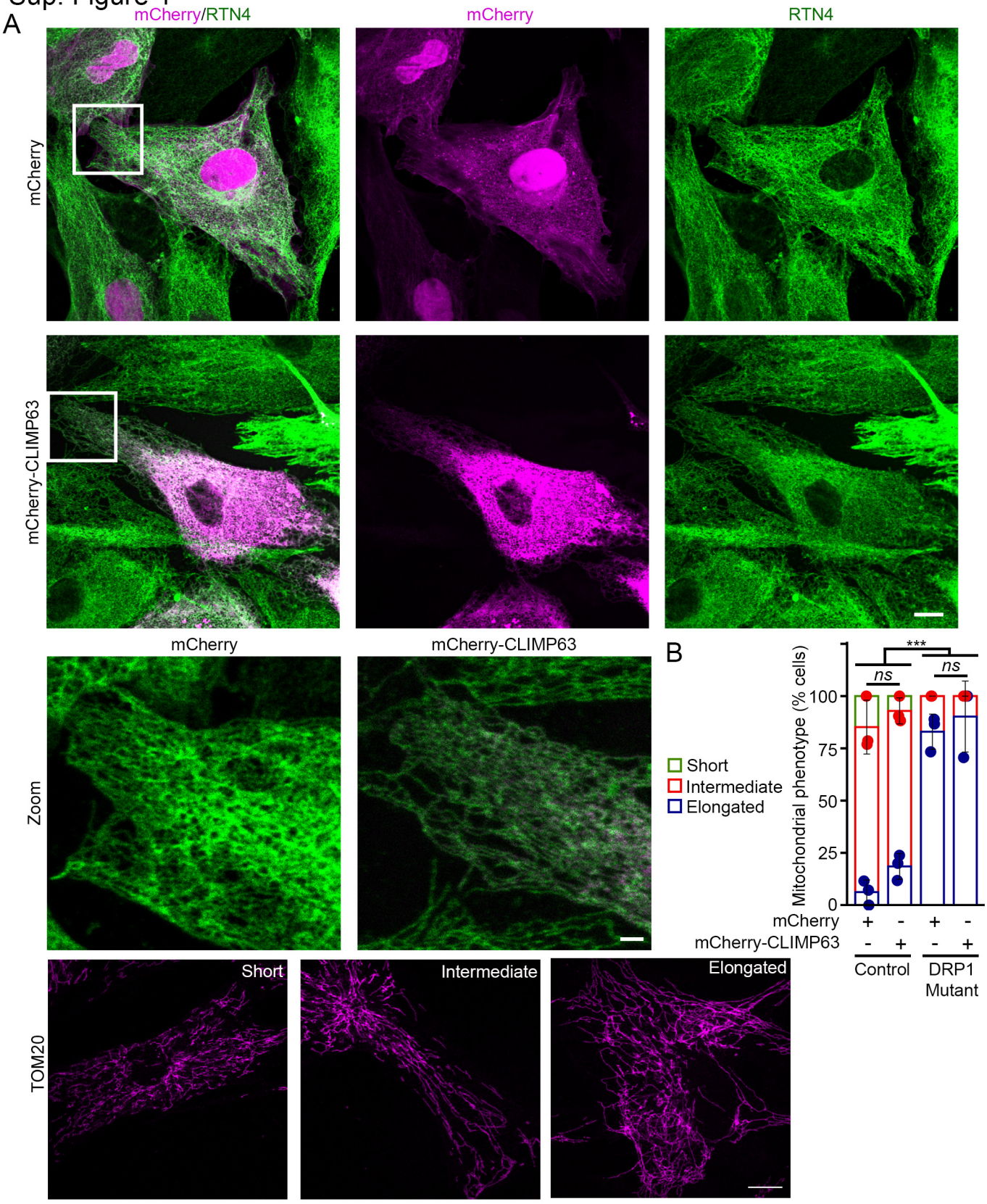

Sup. Figure 5

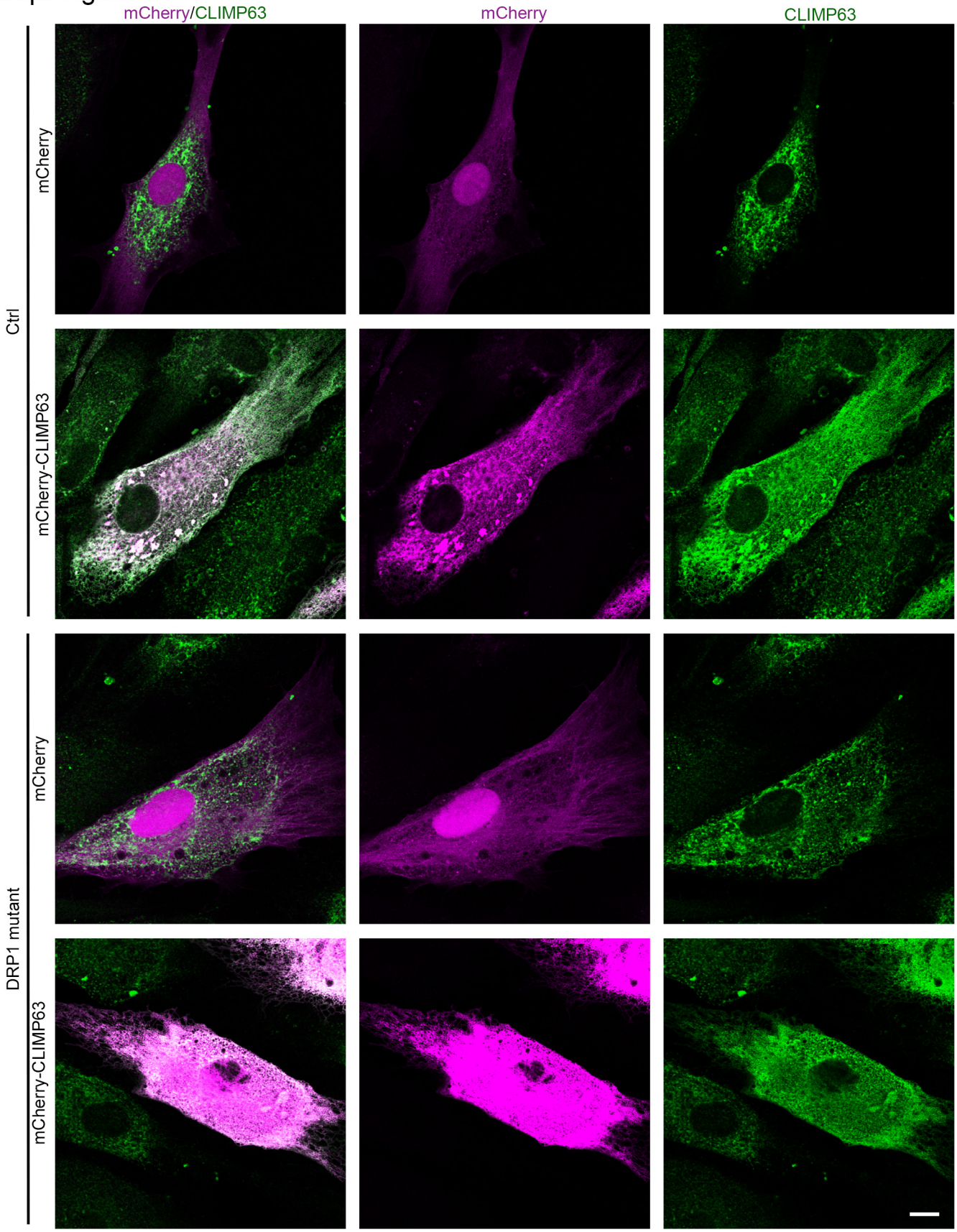

Sup. Figure 6